

Title	Density Functional Investigations on Heme- and Hydrogenase-based Catalysts for Potential Fuel Cell Applications
Author(s)	李, 毅敏
Citation	大阪大学, 2008, 博士論文
Version Type	VoR
URL	https://hdl.handle.net/11094/650
rights	
Note	

Osaka University Knowledge Archive : OUKA

<https://ir.library.osaka-u.ac.jp/>

Osaka University

Density Functional Investigations on
Heme- and Hydrogenase-based Catalysts for
Potential Fuel Cell Applications

「密度汎関数法によるヘム及びヒドロゲナーゼ
の燃料電池電極触媒への適用に関する研究」

2007

Eben Sy Dy

ABSTRACT

Fuel cells are among the most promising alternative power generators of the future. At present, the biggest obstacle to the wide spread use of fuel cells is cost. While fuel cells give excellent value for money in terms of its energy-fuel consumption efficiency, current prototypes are still beyond the purchasing power of the average consumer primarily due to the cost of the precious metal platinum (Pt), which has been the preferred material for anodes and cathodes across most types of fuel cells. Consequently, the quest for alternative catalysts to platinum surfaces that is both efficient and affordable has become a top priority for research around the world in both academia and industry.

Yet contrary to our present platinum-based technology, nature has its own enzymes for oxidizing hydrogen and reducing oxygen without the need for expensive rare metals. With this in mind, we suggested adopting hydrogenase components for hydrogen oxidation reaction (HOR) catalysis and heme components for oxygen reduction reaction (ORR) catalysis.

In this dissertation, HOR/ORR on the platinum surface, the ORR on heme and the HOR on hydrogenase are reviewed. These systems have been extensively studied both experimentally—by spectroscopy, microscopic and electrochemical techniques—and theoretically—by density functional theory (DFT). We then take DFT a step further from its proven applicability in helping us understand HOR/ORR reaction mechanisms to using it as a tool to help us computationally design catalysts as inspired by natural enzymes that perform parallel reactions. The objective of our design efforts for both the anode and cathode is the same: to develop effective and stable alternative electrodes that will eliminate or minimize the use of platinum.

Our design efforts led us to propose Pt deposited on tin (Sn) porphyrin (Por) as an ORR catalyst. The calculated binding energy of Pt on SnPor is 3.13 eV—very stable. We showed how this material possesses the necessary electronic properties that make it a possible alternative to platinum surfaces as fuel cell electrode catalysts; notably: low electron density near Pt, partial negative charge at Pt, and the high Pt-character near and at HOMO (highest occupied molecular orbital) levels. The LUMO (lowest unoccupied molecular orbital) also possess significant Pt d-orbital characteristics comparable to the α - and β -LUMO of iron porphyrin, further suggesting ability to interact with oxygen for catalytic reduction.

We also considered replacing tin with germanium (Ge) and lead (Pb). Pt deposited

on GePor shows primarily the same results as SnPor-Pt, but Pt deposited PbPor shows a much weaker binding energy (1.99 eV). Variants of SnPor-Pt by replacing Pt with nickel (Ni), cobalt (Co), and iron (Fe) were also studied. Our calculations gave energies of 1.29, -0.48 and 0.38 eV respectively for the binding of Fe, Co and Ni on SnPor. We compared their electronic properties with SnPor-Pt, hoping that these non-precious metals on SnPor will also possess the needed electronic properties for fuel cell HOR or ORR catalysis. While the binding energy of Ni on SnPor is not high enough to make SnPor-Ni a viable catalyst for ORR, the similarities between their frontier molecular orbitals suggest that SnPor-Ni may have similar photocatalytic properties as SnPor-Pt for H₂ production in aqueous solution.

For HOR catalysis, on the other hand, we begin our search by studying how changing ligands can affect the electronic structure of the Fe-only hydrogenase active site, the [2Fe]_H subcluster. Density functional theory calculations were performed on Fe-only hydrogenase analogues compounds **I** [(*i*-PDT)Fe₂(CO)₄(CN)₂]²⁻ and **II** [Fe₂(CO)₄{MeSCH₂C(Me)-(CH₂S)₂}(CN)]⁻. Results show electron affinity and trends in molecular orbitals consistent with photoelectron spectroscopy data. The HOMOs show familiar Fe-Fe bonding characteristics while the LUMOs show Fe-Fe antibonding characteristics. To compare the effects of a second CN versus a terminal sulfur ligand, results for **I** after one electron is removed (**I**-1e) were compared with those of **II**. It was found that compound **I**-1e has a much lower HOMO. Mulliken charge analysis also shows that the terminal sulfur has a stronger electron donating effect than a CN ligand. From the standpoint of computational materials design, we therefore think that similarities in electron affinity, 2Fe charge density and HOMO/LUMO energy to the biologically present active site should be bases for predicting catalytic activity.

As a first attempt to hold the [2Fe]_H active site in solid state, we consider thiol derivatives of calixarenes as possible scaffolds. Among the calixarenes so far considered, our calculations have shown that calix[5]arene is the most viable macrocycle to hold the di-iron site. Our calculations also show that the crucial hydrogenase active site is maintained in this material: having an Fe-Fe bond and anti-bond at the HOMO and LUMO respectively; and the bonding orbitals on the Fe centers connected to the sulfur of the electron chain at the HOMO.

TABLE OF CONTENTS

Chapter One.	Introduction	1
Chapter Two.	The Oxidation of Hydrogen and the Reduction of Oxygen on Platinum	4
2.1	The Oxidation of H ₂ on Pt	4
2.2	The Reduction of O ₂ on Pt	5
Chapter Three.	The Oxidation of Hydrogen on Hydrogenase	8
Chapter Four.	The Reduction of Oxygen on Heme	13
Chapter Five.	Methodology	20
5.1	Hartree-Fock Approximation	20
5.2	Density Functional Theory	21
5.3	The Hybrid B3LYP Method	23
5.4	The Basis sets	24
Chapter Six.	Design of Novel Hydrogenase-based Catalyst for HOR	26
6.1	A Density Functional Analysis on the Electronic Properties Fe-Only Hydrogenase Analogues	26
6.2	Hydrogenase Analogue on Calixarenes	31
Chapter Seven.	Design of Novel Heme-based Catalyst for ORR	39
7.1	Depositing Pt on SnPor	41
7.2	Comparing interaction of Pt on SnPor with GePor and PbPor	46
7.3	Interaction of SnPor with other metals	50
7.4	Interaction of SnPor-Pt with O ₂	55
Chapter Eight.	Conclusion	57
References		60
Acknowledgments		
List of Publications		

Chapter One

Introduction

Fuel cells are among the most promising alternative power generators of the future. Unlike boilers and internal combustion engines, they are not constrained by the efficiency limitations of the Carnot cycle. They are compact, quiet, efficient and, thus, suitable for both residential and automotive applications. When used in residences, losses associated with electric transmission from power plants can also be avoided. Furthermore, the heat emitted by fuel cells can be utilized for warming water and/or rooms.

A key player in the field of fuel cells is the hydrogen-fuel PEFC (polymer electrolyte fuel cell), of which a schematic diagram is shown in Figure 1.1. During operation, hydrogen is directed to the fuel cell's anode, which dissociates the incoming gas molecules and strips the atoms of their electrons. This is known as the hydrogen oxidation reaction (HOR). The platinum (Pt) surface has been a popular catalyst choice for this reaction, as experiment and theory agree that the reaction may proceed effortlessly, i.e., the energy barrier for the dissociation of H_2 can be very low. The protons then diffuse along the surface of the anode catalyst, which is another relatively easy process [1-2]. The electron current produced by this reaction powers the external load as the protons diffuse through a membrane made of materials specific to proton conduction, e.g. the polymer Nafion. At the fuel cell's cathode, oxygen combines with the protons from the polymer membrane and the electrons from the external load to form water; this is called the oxygen reduction reaction (ORR). This completes the fuel cell's *catalytic combustion* routine for generating electricity with water being its only by-product. In theory, electricity will continually be generated as long as the hydrogen and air supply does not run out. No green house gas, such as carbon dioxide, is emitted. No toxic carbon monoxide, nitrogen and sulfur oxides are emitted. No carcinogenic incompletely burned fuel is emitted.

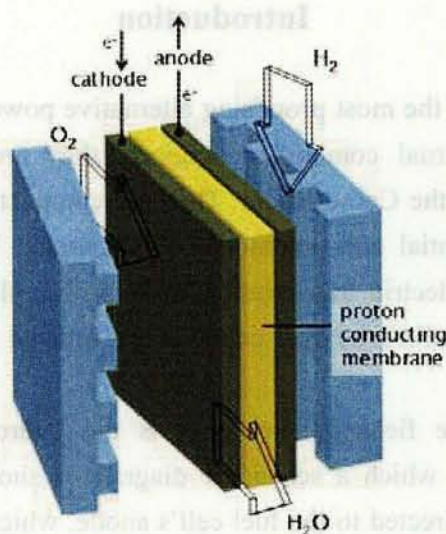


Figure 1.1 Schematic diagram of a fuel cell.

Clearly, a macro-scale understanding of how the fuel cell should work is not a formidable task. However, realizing one fit for mass production is. For Pt-based fuel cells for example, there are performance issues that need to be addressed, such as carbon monoxide poisoning of the electrode catalysts. There are long-term durability difficulties that need to be overcome as well. But ultimately, the biggest obstacle to the widespread use of hydrogen fuel cells is cost. While fuel cells give excellent value for money in terms of its energy-fuel consumption efficiency, current prototypes are still beyond the purchasing power of the average consumer primarily due to the cost of the precious metal Pt, which has been the preferred material for anodes and cathodes across most types of fuel cells.

Because of its vast applications, many studies have been made on how to reduce the amount of platinum in catalysts. They include dispersing platinum nanoparticles in porous silica, alumina and zeolites. But these materials that stably support Pt are not electrically conductive and, therefore, not suitable for electrocatalytic applications such as fuel cells. On the other hand, electrically conductive carbon-based support materials permit Pt nanoparticles to migrate and form larger clusters, leading to reduced catalytic activity over time [3-4].

Yet contrary to our present platinum-based technology, nature has its own way of oxidizing hydrogen and reducing oxygen without the need for expensive rare metals.

With this in mind, we suggested using hydrogenase components for HOR catalysis [5] and heme components [6] for ORR catalysis.

Hydrogenase is a class of enzymes that catalyze the reversible oxidation of molecular hydrogen (H_2), quite similar to what platinum does in fuel cells. It plays a vital role in the metabolism of organisms that can survive in the absence of air. Since their discovery in the 1930s [7], they have attracted the interest of many researchers. Understanding the catalytic mechanism of hydrogenase may help scientists not only design alternative PEFC HOR catalysts but also find clean biological energy sources, such as algae and bacteria that produce hydrogen at viable quantities [7-10]. Heme-containing proteins, on the other hand, perform diverse biological functions including the transportation of oxygen gas, reduction of oxygen molecules and electron transfer. For example, hemoglobin binds oxygen in the lungs where pH is high and pCO_2 is low, travels with blood and releases it in tissues under opposite conditions (where pH is low and pCO_2 is high). The heme iron can also serve as an electron source/acceptor during electron transfer or redox chemistry.

In the following sections, we shall survey literature regarding the ORR and HOR on platinum as well as on heme and hydrogenase. As will be exemplified in these sections, density functional theory (DFT) plays an important role in our current understanding of the ORR and HOR processes, whether as applied in industrially-used platinum-based systems or to biologically-present enzyme systems. From there, we then take DFT a step further from its proven applicability in helping us understand HOR/ORR reaction mechanisms to using it as a tool to help us design catalysts inspired by natural enzymes that perform parallel reactions.

Chapter Two

The Oxidation of Hydrogen and the Reduction of Oxygen on Platinum

At present, platinum surfaces are considered the model electrode catalysts for fuel cells for both the anode, where hydrogen is oxidized into protons (HOR), and cathode, where oxygen is reduced into water (ORR). The HOR and ORR on Pt electrode surfaces are complex subjects affected by factors such as crystal face indices, coverage, vacancies, impurities, environment (e.g. electrolyte used), temperature and pressure. For example, the activity for HOR as a function of crystal face is in the Pt(111)<Pt(100)<Pt(110) [11] order. The HOR reaction is much slower in alkaline solution as compared to acid environment except HX (X=halides) acids. The adsorption of halides as well as hydroxides on Pt surfaces is believed to inhibit H adsorption. Extensive reviews have already been done by Markovic and Ross [12-13].

2.1 The Oxidation of H₂ on Pt

The adsorption of hydrogen on platinum in vacuum has been studied since the 1970's. While these studies are not directly about the oxidation of hydrogen into protons in an electrolyte environment, it does inform us of the possible reactions/interactions between platinum and hydrogen. The adsorption energy of hydrogen in UHV environment is 50-60 kJ/mol (0.52-0.62 eV) on the platinum surface and 70-90 kJ/mol (0.73-0.93 eV) on defect sites [14]. Density functional calculations of Olsen et al. [15] showed little difference between H adsorption energies at various sites of Pt(111). On Pt(100) the reaction is more complex to calculate because H absorption lifts the reconstructed Pt(100) surface [16,17,18]. The heat of adsorption measured by TPD (temperature programmed desorption) is 90-98 kJ/mol (0.93-1.02 eV), which is significantly higher than Pt(111) [19,14]. In our laboratory, we have studied the potential energy surface for dissociative adsorption of H₂ on Pt(111) [2]. The energy barrier is almost zero when the molecular orientation of H₂ is parallel to the surface and when its center of mass is directly above the top site while the H atoms dissociate towards the hcp and fcc hollow sites. Upon dissociation, H atoms isolated at fcc sites can be delocalized by excitation to the first excited state with 30 meV of energy. The subsequent (higher) excited states, which show different migration patterns, are 32-34 meV apart.

All the above studies indicate that the dissociation of hydrogen on platinum proceeds effortlessly, i.e., the energy barrier is very low. This plus the rather weak Pt-H bond makes Pt a very active catalyst for reactions involving hydrogen. However, a weak

Pt-H_{ad} bond also means that Pt can be easily poisoned by strongly adsorbing species (e.g. CO).

The rate of HER/HOR (hydrogen evolution reaction/hydrogen oxidation reaction) on metal surfaces is expressed by the log of exchange current density, $\log i_0$. It exhibits a volcano relationship with the Gibbs energy of hydrogen absorption on the metals (Figure 2.1). The highest i_0 is exhibited by platinum, which sits on top of the volcano curve [20-23]. Norkov et. al. [24] showed a similar volcano relationship between exchange current densities and the calculated hydrogen chemisorption energies by density functional theory. The volcano relationship can be understood as follows: to the left of Pt, H is more and more tightly bonded to the metal surface to be reactive; to the right of Pt, H becomes more and more unstable on the metal surface for H-proton inter-conversion to occur.

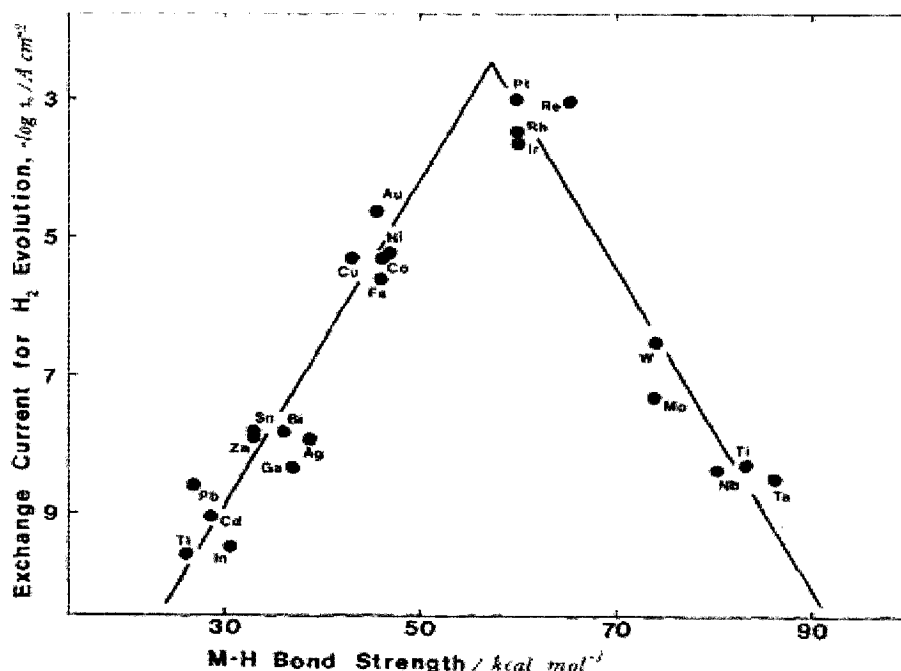


Figure 2.1. Plots of HER/HOR activity versus the binding energy of hydrogen atom on various metals surfaces based on experimental studies. Taken from Ref. [20].

2.2 The Reduction of O₂ on Pt

ORR or the reduction of O₂ on Pt surfaces (and metal surfaces in general) can be simplified [25] as shown in Figure 2.2. K_1 to K_5 represent the reaction rate of each process. Ideally, either K_1 or both K_2 and K_3 should be very high while K_4 and K_5 should be zero—this is called a four-electron reduction process. On the other hand, if K_1 and K_3 are almost zero and K_2 and K_5 are high, a two-electron reduction process

predominates and hydrogen peroxide (H_2O_2) can diffuse into the environment. This degrades the performance of a fuel cell in terms of lower electromotive potential generated and potential damage to the proton transfer membrane.

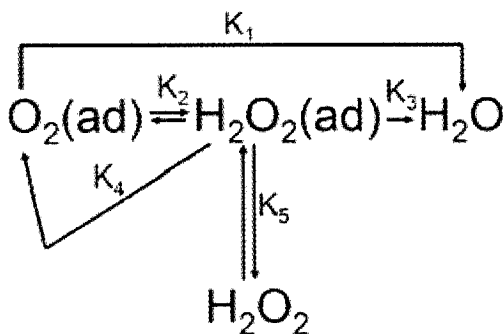


Figure 2.2. Reaction paths for the reduction of O_2 adsorbed on metal surface.

Low pressure experiments (10^{-6} Torr, O_2) have shown that O_2 molecules undergo dissociative adsorption on clean Pt(111) surface at temperatures typical of PEFC operation (80°C). This is opposed to low temperatures (-153°C and below), where molecular adsorption is preferred; the O_2 molecules then dissociate into atoms when heated. At temperatures of around 800°C , a stable oxide is formed [26, 13], but oxygen eventually desorbs at 927°C [13]. Of note, formation of surface oxides leads to reconstruction of the Pt surface. Formation of stable oxides has been shown to poison the catalytic activity of Pt(100) for CO oxidation [27]. While these studies are not directly about the reduction of oxygen into water in a humidified Nafion environment, it does inform us of the possible interactions that oxygen may undergo with the platinum surface.

An ab-initio study by Eichler and Hafner [28] stages the adsorption process into three phases: the physisorbed molecular O_2 , the chemisorbed molecular O_2 , and chemisorbed dissociated atomic O on Pt(111). Their study shows that the chemisorbed O_2 is a paramagnetic superoxo (O_2^-) specie at the bridge site and a diamagnetic peroxo (O_2^{2-}) specie when adsorbed at the three-fold hollow site. Our group, on the other hand, compared the dissociative adsorption of O_2 on two types of Pt surfaces, viz., Pt(001) and Pt(111) by density functional calculations [29]. Of the several factors that may govern O_2 dissociative adsorption, we concentrated on the static effect of surface structure. (Larger distances between Pt atoms exists in the hollow sites of Pt(001) as

compared to Pt(111)). The calculated potential barrier [E_{ac}] for O_2 /Pt(001) [$E_{ac}= 1.2$ eV] is smaller than those for O_2 /Pt(111) [$E_{ac}= 1.7$ eV]. This indicates that O_2 dissociative adsorption occurs much easier on the Pt(001) surface than on the Pt(111) surface, which is also consistent with the activity of Pt(001) for CO oxidation [30-32].

In liquid electrolyte solutions, more complex ORR situations occur due to the competitive adsorption of the electrolyte's anionic species on platinum. Rotating disk electrode (RDE) studies show that relative activity of platinum catalysts varies with crystal face in the order of (111)<<(100)<(110) for sulfuric acid (H_2SO_4), (100)<(110)≈(111) for perchloric acid ($HClO_4$), and (100)<(110)<(111) for potassium hydroxide (KOH). Sulfuric acid was shown to have the strongest deactivating effect. [33]. However, fluorosulfonic acid side-chain of polymer electrolyte membranes (e.g. Nafion) used in modern PEFC's was shown to not interfere with reaction kinetics [34-36].

Recent studies have focused on designing new experimental setups for assessing activity of catalysts in Nafion and in the absence of liquid electrolytes and at temperature and humidity conditions which will simulate the PEFC environment more accurately [37-38]. In one such study, Pt(111) was reported to be twice more active than Pt(100) although details on kinetics or activation energies have not been published at this time [37].

Density functional calculations, particularly those from the groups of Anderson [39-40] and Norskov [41] consider the effects of electromotive potentials on ORR. According to the study of Norskov et. al. [41], OH and O are said to adsorb more stably on Pt surface as the potential (due to the presence of an external load) approaches equilibrium. In the process, the transfer of H^+ and electron to these species becomes more difficult and, in effect, determines the rate of reaction. They popularized what is now known as the "volcano" relationship between the rate of ORR versus the O and OH binding energy on various metals. Pt(111), which sits on top of the activity volcano curve, has binding energies of 1.05 eV and 1.57 eV for OH and O respectively. It would thus also be useful to determine the OH and O binding energy of computationally designed catalysts and fit it into the volcano curve to predict its activity. Of note, their studies suggest that, at high (0.5 ML) O_2 coverage, molecular adsorption of O_2 and reduction via a peroxide mechanism is preferred (at 298°K). A review on *ab initio* calculations done for ORR on metal surfaces was done recently by the group of Wilkinson [42].

Chapter Three

The Oxidation of Hydrogen on Hydrogenase

Hydrogenase is a class of enzyme that catalyzes the reversible $2\text{H}^+ + \text{e}^- \rightleftharpoons \text{H}_2$ reaction in microorganisms. The research in this area is important not only from the view point of understanding biology, but also from the interest in using hydrogen for future energy technologies—organisms could be used to produce commercially viable quantities of H_2 and enzymes can inspire the design of alternative catalysts to platinum. There are two main types of hydrogenases: NiFe and Fe-only; they are named according to the metal/s present in their active site (Figure 3.1). Fe-only and Ni-Fe hydrogenases catalyze the $2\text{H}^+ + \text{e}^- \rightleftharpoons \text{H}_2$ reaction at very high rates [43-44]. However, the catalytic activity of NiFe hydrogenase was realized much later [43], so as a result there are more studies on Fe-only hydrogenase and their analogues in this aspect.

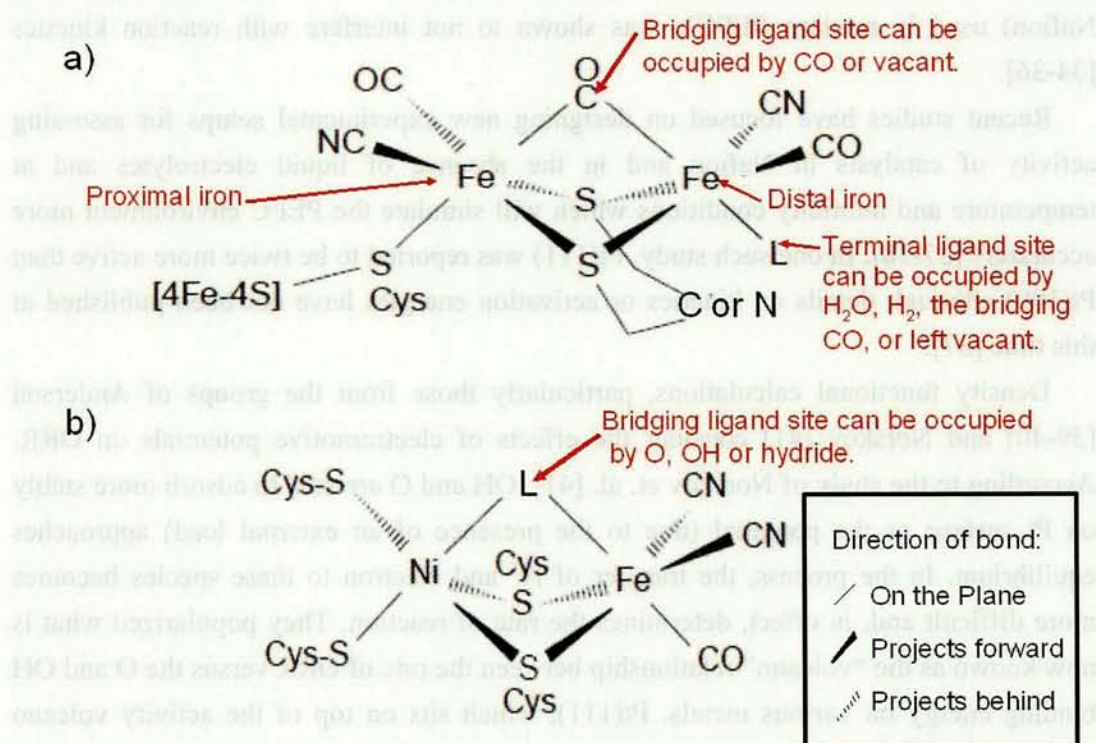


Figure 3.1 Active sites of the two main types of hydrogenases: (a) Fe-only and (b) Ni-Fe. As can be seen in the figure, hydrogenases are named according to the metals present in their active site. S-Cys refers to sulfur from a cysteine amino acid that is connected to the enzymes' polymer chain. Ligands (electron pair donors that bonds to metals; e.g., H_2O , OH, CO) that can change are labeled as L.

The structures of Fe-only hydrogenase from *Desulfovibrio desulfuricans* [45] and *Clostridium pasteurianum* [46] have been characterized by X-ray diffraction. The structure of the former is shown in Figure 3.2. The Fe-only hydrogenase from *Desulfovibrio desulfuricans* contains two sets of iron-sulfur clusters in each protein molecule. The top circle shows the front view while the bottom circle shows the side

view of the iron-sulfur clusters. The right inset zooms into the bottom iron-sulfur cluster (amino acids and hydrogen atoms removed for clarity) which shows the H subcluster (active site) in a dashed circle and the three 4Fe4S clusters that function as a molecular wire (for transporting electron in and out of the protein through oxidation/reduction of the Fe atoms) in dotted circles.

The active site (Figure 3.1a) is an 2Fe3S group also known as the H subcluster, $[2Fe]_H$. The two iron centres are linked through the sulfurs of what is believed to be the anionic form of either 1,3-propane dithiolate (PDT, $^-\text{S}-\text{CH}_2-\text{CH}_2-\text{CH}_2-\text{S}^-$) or dithiomethylamine (DTMA, $^-\text{S}-\text{CH}_2-\text{NH}-\text{CH}_2-\text{S}^-$). Note that PDT and DTMA are identical apart from one carbon being replaced with nitrogen. The “proximal” iron is connected to sulfur from a cysteine amino acid—which is connected to the enzymes’ polymer chain—and subsequently connected to the 4Fe-4S clusters. The distal Fe has a ligand site which can be weakly bonded to H_2O , the bridging CO (the CO at the bridge site between the two Fe atoms can move over to this position), or simply left vacant. (Ligands are electron pair donors that bonds to metals; e.g., H_2O , OH , CO). Each Fe ion in the $[2Fe]_H$ has CN and CO ligands, which interestingly are generally considered poisonous to biological tissues.

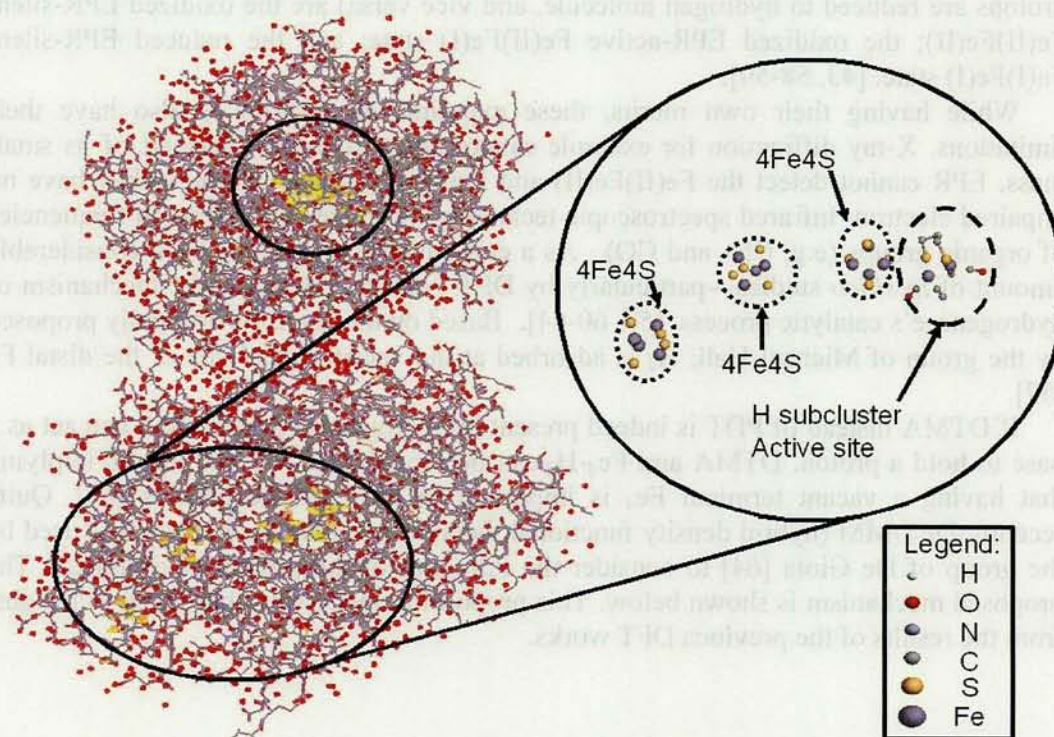


Figure 3.2. The Fe-only hydrogenase from *Desulfovibrio desulfuricans*. Encircled (whole circles) are two complete sets of iron-sulfur clusters contained in each protein molecule. The right inset zooms into the bottom iron-sulfur cluster (amino acids and hydrogen atoms removed for clarity) which shows the H subcluster (active site) in a dashed circle and the three 4Fe4S clusters that function as a molecular wire (for

transporting electrons in and out of the protein through oxidation/reduction of the Fe atoms) in dotted circles.

High quality infrared spectroscopic studies on *Desulfovibrio desulfuricans* confirmed the presence both CN and CO [47] on low spin iron. Of note, FTIR (Fourier transform infrared) spectra of Cpl [48] under cryogenic conditions showed the loss of bridging CO characteristics by light induced reaction, suggesting that the bridging CO moved to distal Fe. Electron paramagnetic resonance (EPR), magnetic circular dichroism (MCD) and Mössbauer spectroscopy, and redox titration studies [49-53] have been performed on Fe-only hydrogenase prior to the elucidation of its structure by X-ray diffraction data. While the experimental results, per se, remain valid, their interpretations have been subject to rethinking based on new insights derived from the crystallographic data. In a more recent EPR study, Popescu and Munck [54] suggested that the two Fe in $[2\text{Fe}]_{\text{H}}$ are in the mixed-valent Fe(III)Fe(II) state while in the active oxidized form, but the Fe(I)Fe(II) state cannot be discounted. On the other hand, investigating “synthetic analogues”—small molecules resembling the H subcluster—by NMR, Mossbauer, FTIR spectroscopy, X-ray diffraction and electroanalytical techniques [55-56] and the original DFT works Cao and Hall [57] led us to the current understanding that the oxidation states the 2Fe group undergo (Fe is oxidized when protons are reduced to hydrogen molecule, and vice versa) are the oxidized EPR-silent Fe(II)Fe(II); the oxidized EPR-active Fe(II)Fe(I) state; and the reduced EPR-silent Fe(I)Fe(I) state. [43, 58-59].

While having their own merits, these experimental techniques also have their limitations. X-ray diffraction for example cannot detect hydrogen because of its small mass. EPR cannot detect the Fe(II)Fe(II) and Fe(I)Fe(I) species because they have no unpaired electron. Infrared spectroscopic techniques measure only vibration frequencies of organic groups (e.g. CN- and CO). As a consequence there have been considerable amount of *in silico* studies—particularly by DFT—set to understand the mechanism of hydrogenase’s catalytic process. [57, 60-64]. Based on mechanisms originally proposed by the group of Michael Hall, H_2 is adsorbed at the vacant ligand site of the distal Fe [57].

If DTMA instead of PDT is indeed present in hydrogenase then DTMA can act as a base to hold a proton. DTMA and $\text{Fe}_d\text{-H}_2$ can become DTMA-H^+ and $\text{Fe}_d\text{-H}^-$ implying that having a vacant terminal Fe_d is important in the catalytic process [60]. Quite recently DFT/MM (hybrid density functional theory-molecular mechanics) was used by the group of De Gioia [64] to consider the influence of the protein environment. The proposed mechanism is shown below. This proposal in many ways has taken in insights from the results of the previous DFT works.

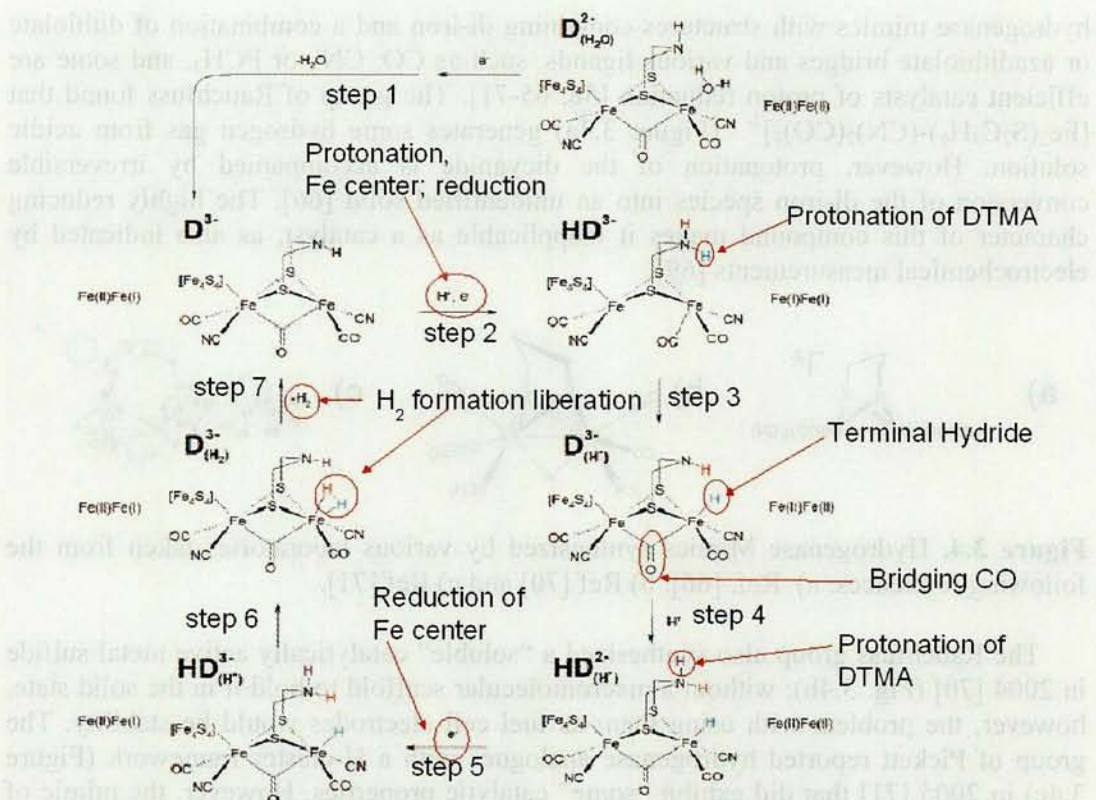


Figure 3.3. Summary HER/HOR reaction mechanism as deduced from DFT/MM (hybrid density functional theory/molecular mechanics) calculation of Ref. [64]. H on the upper right hand side of each figure means that the DTMA is protonated; charge refers to the charge of the entire complex; D means that DTMA was used for modelling (not PDT). Captions added for clarity.

If we follow the arrows in Figure 3.3, we trace the reaction path for the HER (hydrogen evolution reaction), which is simply the reverse reaction of HOR. During enzyme activation (Figure 3.3, step 1), the di-iron center is reduced by one electron from Fe(II)Fe(II) to Fe(II)Fe(I); meanwhile the H₂O ligand of the distal iron is vacated. Subsequently (step 2), the active site then gains another electron and reduces the central di-iron to Fe(I)Fe(I); at the same time, the amine group of DTMA is protonated. The next step (step 3) shows the formation of a hydride on the distal Fe terminal site with the oxidation of the di-iron center to Fe(II)Fe(II); in other words, two electrons were transferred from the Fe(I)Fe(I) to the incoming proton from DTMA. Another proton then attaches to DTMA (step 4) and then another electron reduces the di-iron center back to Fe(II)Fe(I) (step 5). The proton in DTMA and the hydride attached to the terminal position of the distal iron then reacts to form a H₂ (step 6), which eventually evolves off as H₂ gas in the last step (step 7). The cycle (steps 2 to 7) is then repeated and repeated for the reduction of succeeding batches of protons.

The crucial terminal hydride intermediate (also predicted by previous DFT calculations) similar to the one proposed by the above mechanism has recently been identified by NMR spectroscopy at 203 K on an H subcluster active site mimic by Ezzaher et. al [65]. There have been various previous attempts to synthesize

hydrogenase mimics with structures containing di-iron and a combination of dithiolate or azadithiolate bridges and various ligands, such as CO, CN⁻, or PCH₃, and some are efficient catalysts of proton reduction [58, 65-71]. The group of Rauchfuss found that [Fe₂(S₂C₃H₆)-(CN)₂(CO)₄]²⁻ (Figure 3.4a) generates some hydrogen gas from acidic solution. However, protonation of the dicyanide is accompanied by irreversible conversion of the di-iron species into an unidentified solid [66]. The highly reducing character of this compound makes it inapplicable as a catalyst, as also indicated by electrochemical measurements [69].

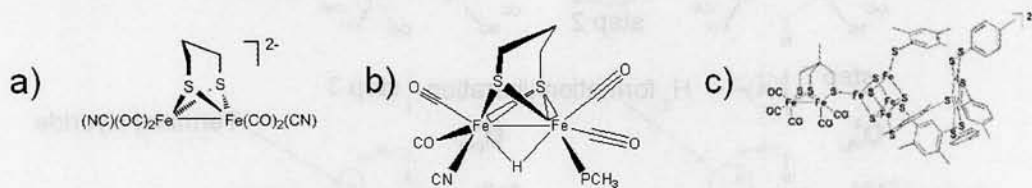


Figure 3.4. Hydrogenase Mimics synthesized by various laboratories taken from the following references: a) Ref. [66], b) Ref [70] and c) Ref [71].

The Rauchfuss group also synthesized a “soluble” catalytically active metal sulfide in 2004 [70] (Fig. 3.4b); without a macromolecular scaffold to hold it in the solid state, however, the problem with using them as fuel cell electrodes would be stability. The group of Pickett reported hydrogenase analogues with a H-cluster framework (Figure 3.4c) in 2005 [71] that did exhibit “some” catalytic properties. However, the mimic of the Pickett group does not have sufficient CN⁻ or equivalent electron donor groups bonded to the Fe-Fe center to make it sufficiently catalytically active. The current state of artificial hydrogenases can be summarized into two groups as: sufficiently active but not sufficiently stable for fuel cell applications, and sufficiently stable but not sufficiently active.

Chapter Four

The Reduction of Oxygen on Heme

Contrary to the present platinum-based technology, nature has its own way of reducing dioxygen without the need for expensive rare metals. With this in mind, we suggested using heme components [6] for fuel cell ORR catalysts. We also performed density functional calculations on a heme-based Fe-porphyrin nanowire, where the adjacent porphyrin macrocycles are linked in parallel, and the result is electrically conductive [72]. Electronic conductivity is a necessary property for fuel cell electrodes to move electrons efficiently. Thus heme-based materials are potential electrode surfaces from the perspectives that it can both conduct electricity and reduce oxygen.

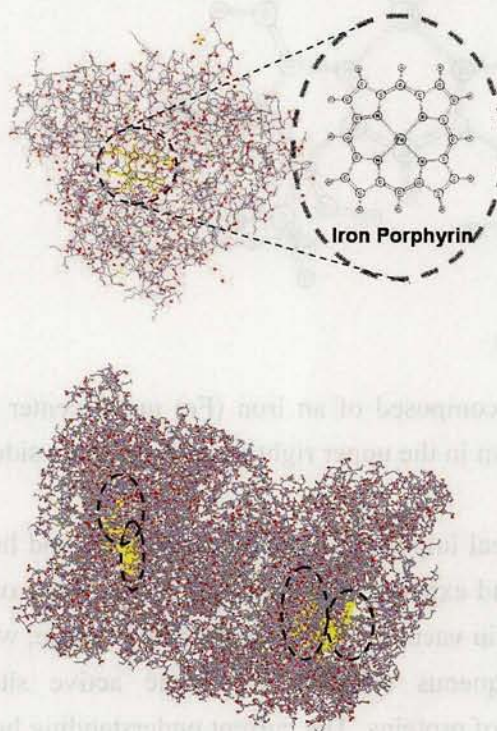


Figure 4.1. Cytochrome P 450 (top) and cytochrome c oxidase (bottom). The heme active sites are highlighted in yellow in broken circles. Cytochrome P 450 has one heme group while cytochrome c oxidase has four heme groups.

Heme occurs in nature as the active site of a variety of biological proteins that interacts with O_2 . Hemoglobin is used to transport oxygen; myoglobin is used for

oxygen transport and storage; cytochrome c oxidase and cytochrome P 450 (Figure 4.1) are used to reduce O_2 . Heme (Figure 4.2) is composed of an iron (Fe) metal center, a porphyrin ring (Por) and some side chains. As shown in the inset of figure 4.2, Por is a planar aromatic macrocycle made of hydrogen, carbon and nitrogen atoms. The Por ring has a net charge of 2- and bonds to the central Fe atom through the four nitrogens. The central Fe atom is commonly found in the 2+ and 3+ oxidation states.

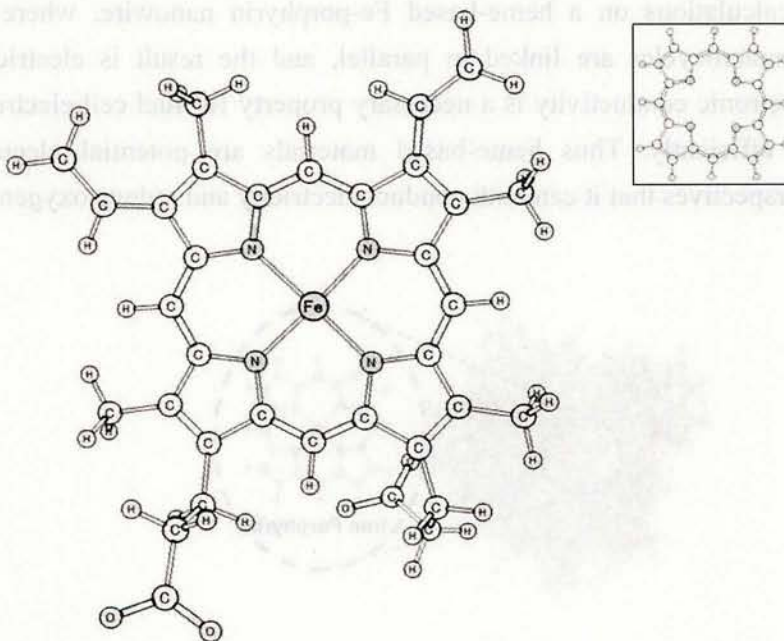


Figure 4.2. Heme is composed of an iron (Fe) metal center enclosed by a porphyrin macrocycle (also shown in the upper right inset) with some side chains.

Due to its biological importance, the reaction of O_2 and heme has been the subject of many theoretical and experimental studies [73-87]. Many of these density functional studies are performed in vacuum. This is justifiable because, while biological molecules naturally exist in aqueous solution, the heme active sites are enclosed within hydrophobic portions of proteins. The current understanding based on literature relevant to our fuel cell ORR concerns can be summarized as follows:

- 1) X-ray diffraction and DFT calculations show that O_2 normally binds to the central Fe atom via an end-on configuration at an Fe-O-O angle of $122-130^\circ$. O_2 pulls the Fe away from the porphyrin plane [79-81]. Electron transfer occurs from Fe to the O_2 in the process. The spin state of Fe changes depending on the ligands

attached. FePor is a triplet and FePor-O₂ is a singlet based on density functional studies [81].

2) We showed that Fe-porphyrin (FePor) and Fe-porphyrin with a histidine (or imidazole) at the fifth ligand site (FePor-Im) has the ability to weaken the O=O bond. However, a histidine bonded to the fifth ligand site suppresses the electronic interaction between Fe and O₂, suggesting that FePor is a better ORR catalyst than FePor-His. On the other hand, we also showed that histidine bonded to the sixth coordination site of Fe can be used to control—specifically, to prevent or activate—the adsorption and desorption of O₂ and other ligands, such as CO and NO [6].

3) A variety of mechanisms for the reduction of O₂ on FePor based molecules has been deduced from Raman spectroscopy, Extended X-ray Absorption Fine Structure (EXAFS) analysis and DFT calculations. Intermediates including the formation of ferric-peroxo (Fe³⁺-O₂⁻), ferric-hydroxy (Fe³⁺-OH) and ferryl-oxo (Fe⁴⁺-O²⁻) complexes have been proposed [82-84].

4) CO can poison FePor. Kinetics studies show that the binding of heme with CO is stronger than that with O₂ by an affinity factor of 20,000, where affinity factor is measured by the ratio of the equilibrium constant for heme with CO over that with O₂ (AF=K_{CO}/K_{O2}). (Equilibrium constant, K, is a measure of how far a reaction goes to completion given particular initial concentrations of heme and O₂ or CO). In hemoglobin and myoglobin, this poisoning effect is minimized by the protein environment to only a CO/O₂ binding affinity factor of 25-270 [85]. The binding energy of O₂ on FePor was computed by density functional theory to be 0.09 eV while that of CO was 0.27 eV [81]. CO binds vertically to the Fe and back donation of Fe d-electrons to the vacant anti-bonding orbitals of CO occurs, consequently enhancing the Fe-CO bond strength. The O₂ in myoglobin is thought to be stabilized by a distal histidine from the protein environment through hydrogen bonding to make it competitive with CO. This is supported by both experimental studies on half-saturation pressures of O₂ ($p_{1/2}^{O_2}$) on heme and their synthetic analogues [82, 79] as well as by DFT calculations [86]. Another contributing factor is that CO is disfavored by steric effects in the protein as CO requires a linear Fe-C-O geometry on FePor, whereas Fe-O-O is bent as earlier mentioned. Collman et al. have synthesized heme analogues with hydrocarbon groups serving as caps over the porphyrin plane. They demonstrated strong

correlation between the porphyrin-to-cap distance and $M(p_{1/2}^{O_2}/p_{1/2}^{CO})$, which is a measure of O_2 versus CO selectivity.

5) The activation barrier for O_2 bond dissociation on FePor at 1.97 eV [6] is higher compared to Pt.

Studies have demonstrated that heme-like compounds adsorbed on or bonded to a carbon support are catalytically active for O_2 reduction [88-91]. Yet none of their prototypes' performance rivals that of the Pt catalyst in terms of stability and efficiency. Logically, the next course of action would be to determine how we can improve on ORR capabilities of heme-based catalysts. We have proposed several ways to achieve these based on density functional calculations.

We consider finding materials which: 1) weaken the O-O bond as evidenced by increase in bond length or decrease in stretching frequency after interaction or 2) lowering of O-O dissociation activation barrier as a first step towards finding alternative ORR catalysts. Early studies involve utilizing physical techniques, such as inducing the side-on interaction of O_2 with FePor [92] (Figure 4.3), to achieve this. The O-O bond of the side-on adsorbed O_2 on FePor- O_2 is relatively weak (1.42 Å versus 1.2 Å of O_2 gas in vacuum), and the side-on O-O bond dissociation barrier (1.35 eV) on FePor is energetically comparable to that of the well-known platinum catalyst as shown in figure 4. We proposed impinging O_2 as oriented- molecular-beams [93-95] aligned to the heme surface to verify our suggestion.

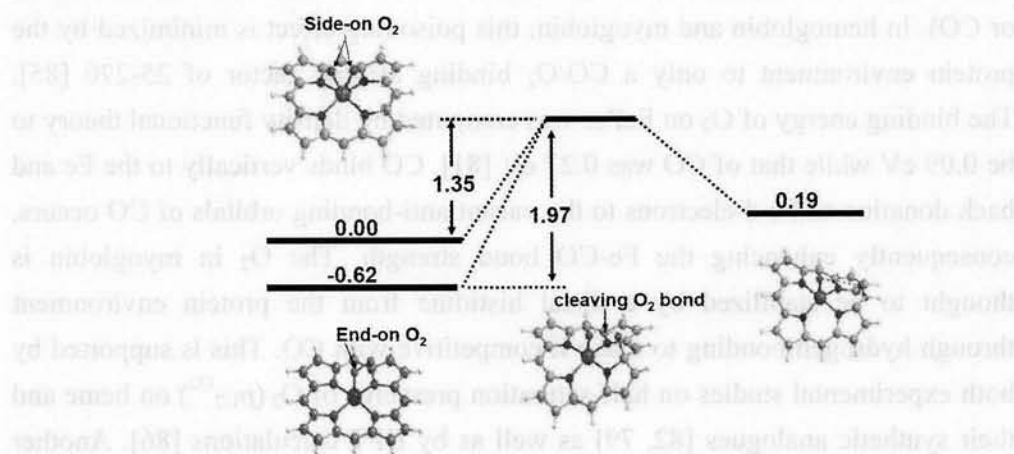


Figure 4.3. The bond dissociation barrier of side-on and end-on O_2 on Fe-Por are 1.35 eV and 1.97 eV respectively.

Another proposal involves magnetizing (Im)FePor- O_2 [FePor- O_2 with an imidazole]

to the triplet state [96] as shown in Figure 4.4. The addition of an imidazole (Im) opposite O_2 on FePor while, at the same time, inducing the triplet state also lowers the activation energy for the dissociation of O-O on heme. The imidazole was said to enhance spin polarization on the Fe and weakening of O-O bond in the triplet state. By inducing the triplet state, the activation barrier for O-O dissociation barrier is lowered to 1.19 eV. We suggested that a strong external magnetic field be applied for this purpose.

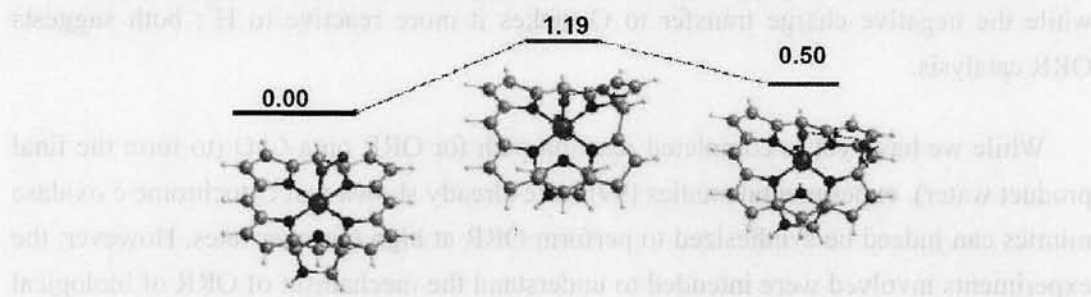


Figure 4.4. Adding an imidazole ligand below the Fe and inducing the triplet state reduced the bond dissociation barrier of O_2 on Fe-Por to 1.19 eV.

While these physical techniques are academically interesting, inducing the triplet state and the side-on interaction are challenging tasks that have yet to be addressed. Furthermore, having to excite heme prior to the catalytic process defeats the idea of designing a more efficient catalyst. Undeniably, the main goal of catalysis is to provide an alternative reaction path with lower energy barriers (due to interaction with the catalyst). Impinging an excited singlet O_2 or applying a strong magnetic field merely added a pre-excitation step to the activation process without lowering the energy of transition state. In other words, it merely changes the reaction from a one-step activation process to a two-step activation process.

Consequently, in our more recent works, we focus on designing new materials, such as Cytochrome c oxidase mimics. Cytochrome c oxidase (CcO) is an enzyme that catalyzes cell respiration in virtually all aerobic organisms. The active site of CcO is a heme-copper binuclear center, where a Cu complex affects O_2 -heme binding and the O-O bond reductive cleavage [97]. The catalytic activity of CcO in biological systems motivated us to evaluate whether a Cu complex would accelerate O_2 dissociation on FePor.

We consider FePor and copper-(imidazole)₃ [Cu(Im)₃] as the representative of the active binuclear center of CcO (Figure 4.5) [98]. The Cu binds to the distal oxygen atom of FePor- O_2 and, in effect, weakens the O-O bond. This is manifested by an increase in

O=O bond length (1.32 Å for FeP-O₂ versus 1.38 Å for FeP-O₂-Cu(Im)₃) and a decrease in O=O stretching frequency (1211 cm⁻¹ to 1082 cm⁻¹). We find that the Cu(Im)₃ weakens the O-O bond primarily by electron transfer to the oxygen atoms. In the FeP-O₂, the charges of the Fe and O₂ are 0.964 and -0.229, respectively. In the FeP-O₂-[Cu(Im)₃], on the other hand, the charges of the Fe and O₂ are 1.531 and -0.717/-0.877, respectively. O₂ bond weakening leads to easier O-O bond dissociation while the negative charge transfer to O makes it more reactive to H⁺; both suggests ORR catalysis.

While we have yet to completed reaction path for ORR on a CcO (to form the final product water), experimental studies [99] have already shown that cytochrome c oxidase mimics can indeed be synthesized to perform ORR at high turnover rates. However, the experiments involved were intended to understand the mechanism of ORR of biological CcO and not performed to simulate PEFC applications.

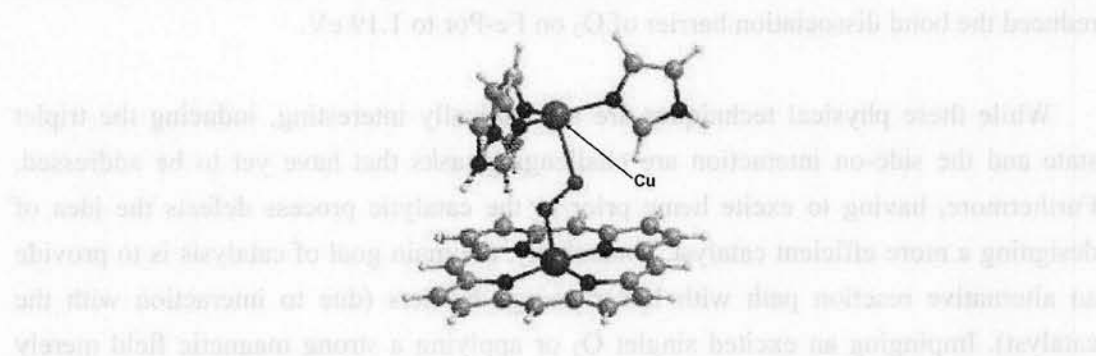


Figure 4.5. The active binuclear center of CcO. The Cu(Im)₃ binds to the distal oxygen atom of FePor-O₂.

We have also considered oxomolybdenum porphyrin, MoO(Por), as a potential ORR catalyst [100]. It has been experimentally shown that the O-O bond increases in length after O₂ is adsorbed on MoO(Por) [101-103]. Our density functional calculations show that the bond length of the adsorbed O₂ is 1.42 Å, much longer than that of gaseous O₂, 1.21 Å. The binding energy of the adsorbed O₂ in MoO(por) (Figure 4.6) is about 0.611 eV, which indicates that the Mo-O bond is weakly stable. In the adsorption process, the electrons in the HOMO of MoO(Por), which are primarily the d-orbitals of the Mo atom, transfer to the π* orbitals of the coming O₂. As an increase in the π* orbitals occupancy and bond lengthening indicates weakening, we think it makes the formation of isolated O atoms for further reaction with protons and electrons to produce the water molecules easier. But due to the low binding energy of O₂ on MoO(por),

applying current to an oxo-molybdenum porphyrin electrode at elevated PEFC temperature will most likely have the same effect as heating or irradiating the said material—i.e., reverse the O_2 adsorption process. Hence, it is quite unlikely that $MoO(por)$ will complete the ORR process because of this reverse reaction. Further design modification $MoO(Por)$ is, therefore, expected to make the use of this catalyst a reality.

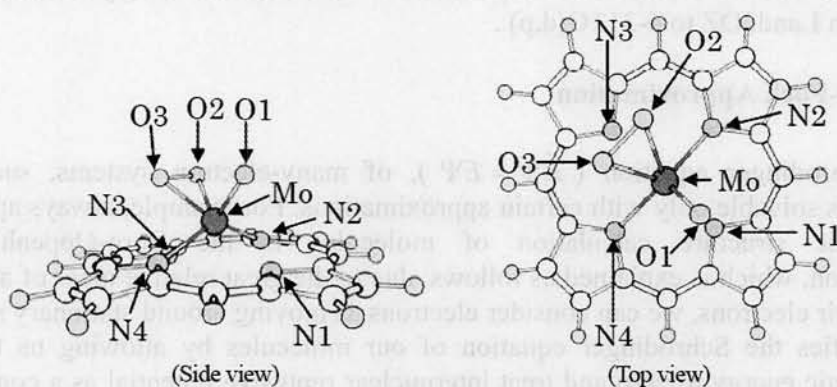


Figure 4.6. O_2 ($O2-O3$) adsorbed on oxomolybdenum porphyrin.

Chapter Five Methodology

The amount of density functional theory (DFT) studies on platinum, heme and hydrogenase discussed in the previous chapters is a testament of its applicability in explaining the HOR and ORR processes. In the subsequent two chapters, we take DFT to the next step by using it, not to explain, but to design and predict the properties of novel heme-based and hydrogenase-based catalyst materials. In this chapter, we introduce the DFT method that was used in our calculations: i.e., Gaussian03 [104] implementation of B3LYP exchange-correlation functional, which is a hybrid of Hartree-Fock, LSDA and GGA methods, with a variety of basis sets ranging from Land2DZ to 6-31+G(d,p) .

5.1 Hartree-Fock Approximation

The Schrodinger equation ($\hat{H}\Psi = E\Psi$), of many-electron systems, such as molecules, is solvable only with certain approximations. For example, always applied in electronic structure calculation of molecules is the Born-Oppenhiemer approximation, which is explained as follows: due to the great relative mass of atomic nuclie to their electrons, we can consider electrons as moving around stationary nuclie. This simplifies the Schrodinger equation of our molecules by allowing us to set nuclear kinetic energy to zero and treat internuclear repulsive potential as a constant. This shortens the Hamiltonians of molecules into so-called “electronic” Hamiltonians:

$$\hat{H}_{elec} = -1/2 \sum_{i=1}^N \nabla^2 - \sum_{i=1}^N \sum_{A=1}^M \frac{Z_A}{r_{ij}} + \sum_{i=1}^N \sum_{j>1}^N \frac{1}{r_{ij}} = \hat{T}_e + \hat{V}_{Ne} + \hat{V}_{ee} \quad (5.1)$$

where the \hat{H} is reduced into three operators that describe: the electronic kinetic energy, the attractive nuclear-electronic potential, interelectronic repulsive potential. In Density Functional Theory, the expectation value of the second term plus the effects of external electric or magnetic fields are collectively referred to as “external potential”.

Perhaps the pivotal approximation that made first principles calculations viable is that of Hartree-Fock [105-106]. The Hartree-Fock approximation is physically sound and computationally possible. The errors of its results are small enough to explain many atomic phenomena although not energetically accurate enough to predict chemical reactions. It approximates the N-electron wave function of atoms (or molecules) as an antisymmetric product of one-electron wave functions $\chi_i(x_i)$, which is a combination of radial and spin functions $\phi(r)\sigma(s)$. The product is called a Slater determinant (Φ_{SD}):

$$\Psi \approx \Phi_{SD} = \frac{1}{\sqrt{N!}} \det \left[\chi_1(\vec{x}_1) \chi_2(\vec{x}_2) \dots \chi_N(\vec{x}_N) \right] \quad (5.2)$$

By expanding the Hartree-Fock determinant and grouping the Hamiltonian into parts: (i|h|j), ((+i|j|j)) and (i|j|i) the expectation value, E_{HF} , can be expressed as:

$$E_{HF} = \langle \Phi_{SD} | \hat{H} | \Phi_{SD} \rangle = \sum_n^N (i | \hat{h} | j) + \frac{1}{2} \sum_i^N \sum_j^N (ii | jj) - (ij | ji) \quad (5.3)$$

where

$$(i | \hat{h} | j) = \int \chi_i^*(\vec{x}_1) \int \left\{ -1/2 \nabla^2 - \sum_A^M \frac{Z_A}{r_{1A}} \right\} \chi_j(\vec{x}_1) d\vec{x}_1 d\vec{x}_i \quad (5.4)$$

contains the Laplacian and the nuclear interaction term,

$$(ii | jj) = \int \int |\chi_i(\vec{x}_1)|^2 \frac{1}{r_{12}} |\chi_j(\vec{x}_2)|^2 d\vec{x}_1 d\vec{x}_2 \quad (5.5)$$

contains the classical electron-electron repulsion term, and,

$$(ij | ji) = \int \int \chi_i(\vec{x}_1) \chi_j^*(\vec{x}_1) \frac{1}{r_{12}} \chi_j(\vec{x}_2) \chi_i^*(\vec{x}_2) d\vec{x}_1 d\vec{x}_2 \quad (5.6)$$

contains the exchange term.

The energy associated with the last term, exchange energy (E_X^{HF}) is entirely a consequence of Pauli's exclusion principle and is mathematically accounted for by the antisymmetry of the Slater determinants. Of note, E_X^{HF} quantity is part of the hybrid B3LYP DFT method. By applying the Euler-Lagrange method of variational calculus to find the lowest energy, a set of Hartree-Fock equations are obtained:

$$\hat{F}(r_1) \phi_i(r_1) = \epsilon_i \phi_i(r_1) \quad (5.7)$$

These equations are solved consistently until the minimum, E_{HF} , is achieved.

5.2 Density functional theory

Superior to the Hartree-Fock approximation is the Density Functional theory (DFT) approach [107-109]. DFT in principle can exactly represent the electronic state of atoms, molecules or solids. The limitation lies only in the approximations of the so-called exchange and correlation energy, (E_{xc}). We encountered exchange energy in the Hartree-Fock approximation. Correlation energy, E_c , on the other hand, is :

$$E_c = E_{\text{ground state}} - E_{HF} \quad (5.8)$$

The Hartree-Fock equation approximates that electrons react with the average potential (χ^2) of the other electrons as shown in equation 5.5. In reality, electrons correlate their movement dynamically trying to avoid each other giving rise to E_c .

DFT is based on the lemma of Hohenberg and Kohn [107] which states that the ground state density, $n(r)$, of a quantum mechanical system determines the external potential, $v(r)$, uniquely to within an additive constant C :

$$n(r) \rightarrow \text{unique } v(r).$$

Integrating $n(r)$ determines N (i.e. total electrons of the system) thus, the Hamiltonian of the system and, hence, all properties that can be determined from the Hamiltonian. From this lemma, energy as a functional of $n(r)$ can be determined variationally with trial wave functions, $\Psi[n(r)]$.

$$E_{v(r)}[n(r)] \equiv \int v(r)n(r) dr + F[n(r)] \quad (5.9)$$

where $F[n(r)]$ in its practical form [110] is

$$F[n(r)] = T[n(r)] + 1/2 \int \frac{n(r)n(r')}{|r-r'|} dr dr' + E_{xc}[n(r)] \quad (5.10)$$

The energy of the ground state can be solved variationally as:

$$E_{v(r)}[n(r)] \geq E_{v(r)}[n_0(r)] \equiv E \quad (5.11)$$

If E_{xc} is replaced with E_x (and E_c is ignored), the physical meaning of these equations is the same as the Hartree-Fock approximation. Similarly, $E_{v(r)}[n(r)]$ also have the following associated Euler-Lagrange equation, better known as the Kohn-Sham [108] equations:

$$\left(-\frac{1}{2} \nabla^2 + v(r) + \int \frac{n(r')}{|r-r'|} dr' + v_{xc}(r) - \epsilon_j\right) \phi_j(r) = 0 \quad (5.12a)$$

$$n(r) = \sum_{j=1}^N |\phi_j(r)|^2 \quad (5.12b)$$

$$v_{xc}(r) = \delta E_{xc}[n(r)] / \delta n(r) \quad (5.12c)$$

These equations are solved self-consistently like in the Hartree-Fock approach with an additional V_{xc} term instead of V_x only. However, while the additional computational resources necessitated by adding the V_{xc} is rather minimal, the quality of results generated by DFT is greatly enhanced over HF in terms of the accuracy.

In our studies, the unique external potential $v(r)$ is set by the position and charges of the atomic nuclei of the molecules of interest. The total numbers of electrons of our molecules, N , are also known. We solve the Kohn-Sham equations by systematically varying coefficients our basis sets (discussed below) to determine: total electronic energy of the molecules in the ground state ($E[n(r)]$), orbital energies (ϵ_j) and wave function (ϕ_j) of each electron, total electron density distribution ($n(r)$) and, from there, vibrational force constants of chemical bonds and charge distribution in the molecule.

The simplest approximation for exchange and correlation energy is the local density approximation, LDA, and its spin-dependent version, LSDA, which is based on the assumption that

$$E_{xc}^{LDA}[n] = \int n(r) \epsilon_{xc}(n(r)) dr \quad (5.13)$$

, where $\epsilon_{xc}(n(r))$ is exchange-correlation energy per electron, $\epsilon_{xc} = \epsilon_x + \epsilon_c$. The exchange energy, ϵ_x , of each electron, in LDA is based on the exchange energy of a homogeneous electron gas of density, n , which has a quite well-known form

$$\epsilon_x = -\frac{3}{4} \left(\frac{3n(r)}{\pi} \right)^{1/3} \quad (5.14)$$

leading to

$$E_x^{LSDA} = -3/2 \left(\frac{3}{4} \pi \right)^{1/3} \sum \int n_\sigma^{4/3} dr \quad (5.15).$$

Correlation energy, ϵ_c , on the other hand, such as that suggested by Vosko, Wilk and Nusair [111] is an analytical expression derived from Monte Carlo Simulations of a uniform electron gas done by Ceperly and Alder [112]. But while a uniform electron gas reasonably represents the valence electrons of metal surfaces, it does not do so for molecular systems.

A drastic improvement over the LDA approach is the GGA or Generalized Gradient approximation where exchange and correlation energy is not considered only a functional of $n(r)$ but also its gradient, $\nabla n(r)$. Becke [113] found an exchange GGA that reproduces the asymptotic behavior of exchange energy expressed as:

$$E_x^{Beck88} = E_x^{LSDA} - b \sum_{\sigma} \int d\mathbf{r} \, n_{\sigma}^{4/3} \frac{X_{\sigma}^2}{(1 + 6b X_{\sigma} \sinh^{-1} X_{\sigma})} \quad (5.16)$$

where E_x^{LSDA} is the exchange energy by the local spin-density approximation (spin-dependent version of LDA),

$X_{\sigma} = |\nabla n_{\sigma}| / n_{\sigma}^{4/3}$ is gradient correction of exchange term, and,

b is an empirically fitted constant, -.0042 a.u.

Another popular exchange functional was introduced by Perdew in 1986 [114]. Perdew 1986 is free of any empirical parameters and has been a popular choice for studying solids, while Beck3 1988 remains the choice for molecular calculations.

For correlation functionals, the consequences of applying GGA are also significant. The most popular GGA correlation functional being used for molecular systems are LYP (Lee-Yang-Parr) [115], P86 (Perdew 1986) [116] and PW91 (Perdew and Wang 1991)[117].

5.3 The Hybrid B3LYP Method

Generally, GGA gives reliable results for all main types of chemical bonds, except van der Waals interaction. Nevertheless, the search for more accurate functionals continues. Perhaps, one of the most successful is the use of hybrid functionals. Hybrid functionals mix a fraction of Hartree-Fock exchange with DFT exchange functionals and a fraction of local correlation with gradient-corrected functional. The mixing involves empirically established weight factors, which may seem to be a drawback theoretically but has been proven to be advantageous practically over the past years.

The B3LYP method was first implemented by Dr. M. J. Frisch of what is now Gaussian, Inc. in 1994 to explain vibrational absorption and circular dichroism spectra of 4-methyl-2-oxetanone, obtained by the group of Prof. P. J. Stephens at the University of Southern California [118]. At that time, Becke [119] has just introduced the "hybrid" functionals, Hartree-Fock results were known to be insufficiently accurate and MP2 (Moeller-Plesset 2nd order perturbation theory) was too computationally expensive. After evaluating a variety of exchange and correlation functionals, B3LYP turned out clearly superior over HF, LSDA, BLYP. Subsequent studies have also shown B3LYP to be appropriate for molecular systems, including heme and hydrogenase [57, 64, 80].

The B3LYP exchange and correlation energy is expressed as a combination (or a "hybrid") of local and gradient-corrected exchange/correlation terms and the exact Hartree-Fock exchange term. It is implemented in Gaussian 03 as shown below:

$$E_x^{B3LYP} = (1 - a_0) E_x^{LSDA} + a_0 E_x^{HF} - a_x \Delta E_x^{SS} + a_c E_x^{LYP} + (1 - a_c) E_x^{P86} \quad (5.17)$$

where E_{xc}^{B3LYP} is B3LYP exchange-correlation energy term,

a_0, a_x, a_c are parameters determined by Becke to be 0.2, 0.72, 0.81 from experimental heats of formation of small molecules,

E_x^{LSDA} is the local spin-density exchange functional energy term
 E_x^{HF} is the exact Hartree-Fock exchange energy term
 ΔE_x^{B88} is Becke's gradient correction to the exchange energy term.
 E_c^{LYP} is the Lee-Yang-Parr correlation energy term which includes density gradient terms, and,
 E_c^{VWN} is the local correlation energy term of Vosko, Wilk and Nusair.

Most of the calculations we did were performed with B3LYP except for section 6.1. (A Density Functional Analysis on the Electronic Properties Fe-Only Hydrogenase Analogues) where the BPW91 pure DFT method yielded better results than B3LYP. BPW91 uses Becke 1988 for exchange and Perdew-Wang 1991 for correlation. The term “pure” is used to differentiate “B” from “B3”, which in contrast is a “hybrid” of DFT and Hartree-Fock exchange.

5.4 The Basis Sets

When atoms cluster together into molecules, electrons (especially the valence ones) do not isolate themselves to their respective nucleus. On the contrary, they interact with all nuclei and electrons in the molecule. The new electronic states which are formed when atoms cluster into molecules are called “molecular orbitals”. The numerical solution of the Kohn-Sham equation is performed by expanding the molecular orbitals as a set of suitable basis functions and solving the resulting equation by varying coefficients of this expansion until energy is minimized to a convergence factor of 10^{-5} (normal, used in geometry optimization) or 10^{-10} (tight, used for determining energy of the system). One can approximate the molecular orbitals as a Linear Combination of Atomic Orbitals (LCAO). In the LCAO approach, each one-electron molecular orbital (ϕ_i) is approximated as the sum of all atomic orbitals in the molecule multiplied by a constant factor, c , as shown in equation below:

$$\phi_i = \sum_r c_{ri} \chi_r \quad (5.18)$$

where the coefficients, C_{ri} are determined self-consistently.

The collection of one-electron wave functions, χ , plus its corresponding nuclear potential, Z , of an atom is called its basis set. In Gaussian 03, one-electron wavefunctions are represented by a combination of gaussian functions, G , to fit Slater functions, S . (Slater type trial functions were shown to describe atomic orbitals well but are much harder to converge computationally than Gaussian functions.)

$$S_{nlm}(r, \theta, \phi) = N_n r^{n-1} e^{-\zeta r} Y_l^m(\theta, \phi) \quad (5.19)$$

where N_n is normalization constant $= (2\zeta)^{n+1/2} / [(2n)!]^{1/2}$

$Y_l^m(\theta, \phi)$ are the spherical harmonics

ζ , zeta, is a variationally determined parameter

$$S_{nlm}(r, \theta, \phi) \approx \sum d_{nlm} G_{nlm}(r, \theta, \phi) \quad (5.20)$$

where d_{nlm} are chosen to fit a Slater function, and,

G_{nlm} is $N_n r^{n-1} e^{-\alpha r^2} Y_{lm}(\theta, \phi)$ where the α 's are also used to fit the Gaussian functions into a Slater function.

Some basis sets contain the wave functions for all its electrons and a potential to represent the nucleus; these are called “all-electron” basis sets. Others contain only the valence electrons, and the inner electrons are considered together with the nucleus as an effective nuclear charge, which is called a “psuedocore” potential. Basis sets with psuedocore potentials are useful for big atoms, so as not to overwhelm the computers with too much electron wavefunctions. This is a valid approach since inner core electrons are known not to contribute to chemical bonding anyway.

Aside from the number of atoms in a molecule and the number of electrons of each atom, another factor that contributes to the amount of the computational resources needed is the “size” of the basis set, i.e., how many Gaussian functions are used to describe each electron. Bigger basis sets use more Gaussian functions and approximates the wave functions of electrons more accurately but requires greater computational resources. In our case, we use the smallest basis set that can accurately predict geometry (~2-3% error), vibrational frequencies (IR or Raman ~50 cm⁻¹ error) and/or vertical detachment energy (~0.15 eV error) depending on availability of experimental data of related compounds, such as synthesized heme- and hydrogenase-mimics.

For our hydrogenase studies, we find the 6-31+G(d,p) and 6-311+G(d,p) [121] basis sets appropriate. Both 6-31+G(d,p) and 6-311+G(d,p) basis sets use six Gaussian functions to fit one Slater function for inner electrons. For valence electrons, 6-31+G(d,p) uses two Slater functions (double zeta); three and one Gaussian functions are used to fit the two Slater functions, respectively. On the other hand, 6-311+G(d,p) uses three Slater functions (triple zeta) for valence electrons; three, one and one Gaussian functions are used to fit the three Slater functions, respectively. “(s,p)” (polarized basis set) indicates that additional Gaussian functions with angular momentum higher than the ground-state configuration were included to allow atomic orbitals to change shape. For example, in the case of carbon, (d,p) denotes a d-function added to p-orbitals; in the case of hydrogen, (d,p) denotes a p-function added to s-orbitals. + (diffused basis set) indicates the addition of a Gaussian function with a small exponent to allow electron density to spread out. For the design of heme-based catalysts, we find the LanLD2Z [122] basis set appropriate. LanLD2Z uses the double zeta functions for C, H and N, and the Los Alamos pseudo-core potential plus double zeta functions for Pt, Fe, Co, Ni, Ge, Pb and Sn.

Chapter Six

Design of Novel Hydrogenase-based Catalyst for HOR

With heme, our preferred nature-inspired alternative ORR catalyst, the active metal is housed in the organic macrocyclic, porphyrin. Aside from perturbing the electronic properties of iron in a positive way, porphyrin furnishes the metal active center with a desirable solid state environment making it suitable for heterogeneous catalytic processes (oxygen is in the gaseous state while the electrodes must remain in the solid state). Fe-porphyrins, for example, can be readily mixed with graphite materials and even heat treated to make a fuel cell cathode [42]. The Fe-only hydrogenase active site, $[2\text{Fe}]_{\text{H}}$ subcluster (Figure 6.1a), which is highly soluble in water, on the other hand is not as fortunate. The design of a $[2\text{Fe}]_{\text{H}}$ analogue on solid state support (scaffold) that maintains its catalytic activity is therefore necessary. This is a challenging task since the hydrogenase active site is 3-dimensional (unlike heme, which is planar) and binuclear (two irons). Furthermore, the origin of its catalytic behavior is not well understood.

6.1. A Density Functional Analysis on the Electronic Properties Fe-Only Hydrogenase Analogues

We first considered using hydrogenase as a potential anode material in 2005 [5]. Our calculations show that the dissociation barrier of H-H on the hydrogenase active site can be as low as 0.05 eV. To further investigate the nature of the $[2\text{Fe}]_{\text{H}}$ subcluster, we now studied the electronic structure of two hydrogenase analogues [122]—compounds **I** $[(i\text{-PDT})\text{Fe}_2(\text{CO})_4(\text{CN})_2]^{2-}$ and **II** $[\text{Fe}_2(\text{CO})_4\{\text{MeSCH}_2\text{C}(\text{Me})-(\text{CH}_2\text{S})_2\}(\text{CN})]^{-1}$ —by density functional theory. The structure of compounds **I** and **II** are shown in Figures 6.1b and 6.1c.

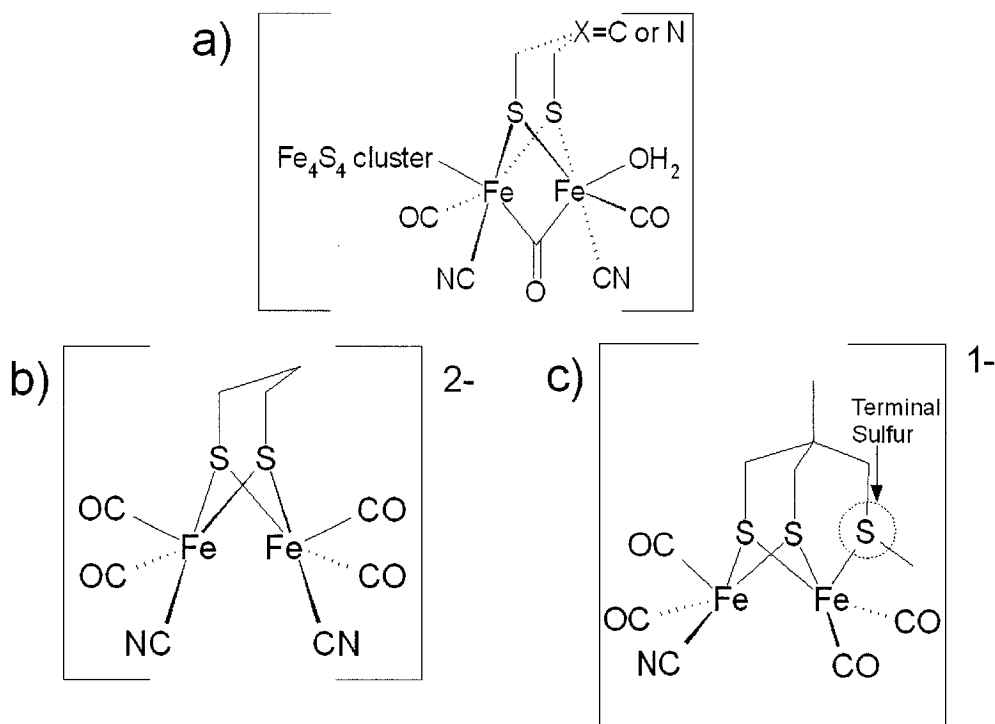


Figure 6.1. The active site of Fe-only hydrogenase, the $[2Fe]_H$ subcluster (a), and its synthetic analogues $[(i-PDT)Fe_2(CO)_4(CN)_2]^{2-}$ (b) and $[Fe_2(CO)_4\{MeSCH_2C(Me)-(CH_2S)_2\}(CN)]^{1-}$ (c). We refer to (b) and (c) as compounds **I** and **II**, respectively, and the encircled sulfur in (c) as the terminal sulfur ligand.

Results are compared with electron affinities and molecular orbital energies obtained by Gas-phase photodetachment photoelectron spectroscopy (PES) in the previous work by Yang *et al* [123]. While PES is an outstanding tool to study the electronic structure, we are re-visiting these results due to the current availability of more sophisticated computational tools. Electron affinity, a measure of ion and free radical stability, is important in the electronic transfer and reactions of biological processes. An accurate description of the electronic structure of the $2Fe_3S$ hydrogenase analogues is of key importance in our efforts to understand its catalytic behavior and design new HER/HOR catalytic materials.

We modeled and performed spin-restricted density functional calculations on compounds **I** and **II**, in the singlet ground state as implemented in GAUSSIAN 03[104]. While there were actually five compounds studied by Yang *et. al* [123], three were not considered due to the similarity of their bonding at the iron centers and of their PES experimental results to the two compounds studied herein. Full geometry optimization

was performed using 6-31+G(d,p) with the three parameter Becke/Lee–Yang–Parr (B3LYP) hybrid DFT functionals and Becke/Perdew-Wang (BPW91) pure DFT functionals for our exchange-correlation functionals. For single-point energy, calculations were also performed with 6-311+G(d,p), 6-311++G(d,p) basis sets with B3LYP and BPW91.

For Electron affinity (EA), or more precisely the Adiabatic Detachment Energy (ADE), spin-unrestricted single point energy calculations were performed on $[(i\text{-PDT})\text{Fe}_2(\text{CO})_4(\text{CN})_2]^{1-}$ and $[\text{Fe}_2(\text{CO})_4\{\text{MeSCH}_2\text{C}(\text{Me})-(\text{CH}_2\text{S})_2\}(\text{CN})]^{0-}$ based on the relaxed geometry obtained for $[(i\text{-PDT})\text{Fe}_2(\text{CO})_4(\text{CN})_2]^{2-}$ and $[\text{Fe}_2(\text{CO})_4\{\text{MeSCH}_2\text{C}(\text{Me})-(\text{CH}_2\text{S})_2\}(\text{CN})]^{1-}$, respectively. Geometry optimization was not performed in consideration of the Franck-Condon factor. Electron affinity is computed as: $\text{EA}_{\text{ADE}} = E(\text{optimized anion}) - E(\text{single-point calc. anion} + 1)$ [124].

We compare the Adiabatic Detachment Energy from our DFT calculations with PES data as shown in Table 6.1. We found that 6-311+G(d,p) yields result comparable to the bigger 6-311++G(d,p) basis sets. B3LYP exchange and correlation functionals tend to slightly underestimate the EA, while BPW91 tends to slightly overestimate it. With spin unrestricted calculations however, spin contamination was significantly larger for B3LYP (~16%) than BPW91 (~2%). All results are well within the expected ± 0.2 eV [124] of the experimental value of 1.5 and 3.3 eV for compounds **I** and **II**, respectively.

Table 6.1. Comparison of Electron Affinity (ADE) values in eV for compounds **I** and **II** obtained by DFT calculation [using B3LYP and BPW91 with 6-31+G(d,p), 6-311+G(d,p) and 6-311++G(d,p)] versus experimental PES technique from Ref. 123.

	Compound I $[(i\text{-PDT})\text{Fe}_2(\text{CO})_4(\text{CN})_2]$		Compound II $[\text{Fe}_2(\text{CO})_4\{\text{MeSCH}_2\text{C}(\text{Me})-(\text{CH}_2\text{S})_2\}(\text{CN})]^{1-}$	
	B3LYP	BPW91	B3LYP	BPW91
6-31+G(d,p)	0.071	0.302	3.234	3.401
6-311+G(d,p)	-0.002	0.256	3.168	3.418
6-311++G(d,p)	0.064	0.229	3.236	3.420
Expt'l EA [123]	0.15	0.15	3.3	3.3

The molecular orbital energies from our BPW91/6-311+G(d,p) calculation are now reported. Molecular orbitals obtained with smaller basis sets [BPW91/6-31+G(d,p) and B3LYP/6-31+G(d,p)] do not show significantly different results for spin restricted systems, while molecular orbitals of the bigger basis set calculations cannot be retrieved for B3LYP due to memory limitations. Nevertheless, our results and the PES data obtained by Yang *et al* showed consistent trends. Specifically, energy regions of molecular orbitals in our calculation corresponds well to the bands in the PES spectra,

and energy gaps with no molecular orbitals present coincides well with valleys in the PES spectra. The energy of the molecular orbitals and their corresponding regions in the PES are shown in Table 6.2. For **I**, the near HOMO levels cannot be seen in the PES because they are positive values. For **II**, the near HOMO region can be seen as predicted our DFT calculations in the PES but the signal is weak indicating the wavelength (157 nm) used could too high for this region.

Table 6.2. Comparison of the BPW91/6-311+G(d,p) molecular orbital energies with photoelectron spectra obtained by Yang *et al* [123]. Energy regions of molecular orbitals in our calculation corresponds well to the bands in the photoelectron spectra, while energy gaps with no molecular orbitals present coincides with valleys in the spectra.

Compound I [(i-PDT)Fe ₂ (CO) ₄ (CN) ₂] ²⁻			Compound II Fe ₂ (CO) ₄ {MeSCH ₂ C(Me)-(CH ₂ S) ₂ }(CN)] ⁻		
MO no.	Energy (eV)	PES region	MO no.	Energy (eV)	PES region
	(1 eV gap)		71	-8.5	
55-58	-7.4 to -6.9	D band	72	-8.4	
	(1 eV gap)		73	-8.1	
59	-5.9		74-88	-7.8 to -6.8	B band
60	-5.5	C band	89-93	-6.4 to 6.0	A band
61-75	-4.8 to -3.4	B band		(0.4eV gap)	
76-78	-3.2 to -2.9	A band	94	-5.5	
	(0.6 eV gap)			(0.8 eV gap)	
79	-2.3		95	-4.8	
	(0.8 eV gap)		96-102	-4.4 to -3.0	X band
80	-1.5			(0.6eV gap)	
81-88	-2.05 to 0.0	X and	103-108	-2.4 to -1.7	Weak signals
89-95	0.19 to 1.5	Cannot be seen by PES	109	-1.43 (HOMO)	
96	1.76 (HOMO)				

Wave functions of the HOMO and LUMO are plotted in Figure 6.2. As can be seen in the figure, electrons in each orbital are delocalized between the iron centers and the ligands. The Fe-Fe bonding and anti-bonding are still clearly seen for the HOMO and LUMO respectively as described for Fe₂S₂CO₆ clusters [125]. The other near HOMO-LUMO wave functions (not shown) all possessed iron properties; orbitals with predominantly ligand characteristics are not seen.

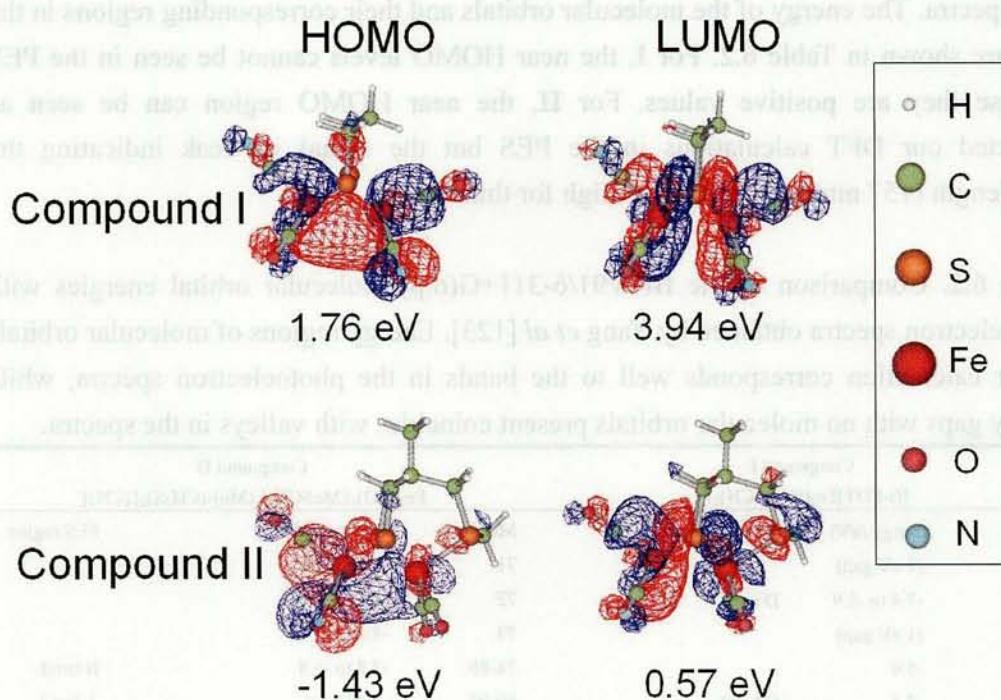


Figure 6.2. The HOMO and LUMO wave functions of compounds $[(i\text{-PDT})\text{Fe}_2(\text{CO})_4(\text{CN})_2]^{2-}$ **I** and $[\text{Fe}_2(\text{CO})_4\{\text{MeSCH}_2\text{C}(\text{Me})-(\text{CH}_2\text{S})_2\}(\text{CN})]^-$ **II**, and their corresponding energy (eV).

In **II**, it can be seen that HOMO electrons also cover the terminal sulfur. This corroborates the works of Schwab *et al.* [126] that the $[2\text{Fe}]_{\text{H}}$ subcluster and the neighboring $4\text{Fe}4\text{S}$ cluster found in biological systems, should actually be designated as an electronically inseparable $6\text{Fe}6\text{S}$. This, however, does not imply that only $[2\text{Fe}]_{\text{H}}$ subcluster analogues with $4\text{Fe}4\text{S}$ analogues will be catalytically active to HER/HOR; indeed, Gloaguen *et al.* [70] has also shown that replacing a cyanide group in compound **I** with CH_3P results in a catalytically active compound.

The HOMO energy of **I** is much higher than that of **II**, which is understandable because **I** is in the -2 anionic state *cf* -1 for **II**. To compare the effects of ligands—specifically, a second CN versus a terminal sulfur ligand—results for compound **I** after one electron is removed $[(i\text{-PDT})\text{Fe}_2(\text{CO})_4(\text{CN})_2]^{1-}$ or “compound **I-le**” were compared with compound **II**. We found that **I-le** has a much lower HOMO at -3.7 eV versus -1.43 eV for **II**, even if their 2Fe centers have the same oxidation states. Mulliken charge analysis also shows that the terminal sulfur has a stronger

electron donating effect than CN ligand with 2Fe charges of 4.88 for I-1e and 4.66 for II.

From the standpoint of computational materials design, it can be seen that changing ligands will primarily affect the charge distribution and HOMO/LUMO wave function/energy levels of 2Fe2S clusters. We therefore think that similarities in electron affinity, 2Fe charge density and HOMO/LUMO characteristics to the biologically present active site should be bases for predicting catalytic activity of Fe-only hydrogenase analogues. With this systematic knowledge, we will be able to design and predict the catalytic activity of theoretical [2Fe]_H analogues even before they are actually synthesized.

6.2 Hydrogenase Analogue on Calixarenes

As a first attempt, we consider thiol derivatives of calixarenes (i.e, replacing the –OH groups with –SH groups) as possible scaffolds to hold the [2Fe]_H active site in solid state [126]. Calixarenes are cyclic oligomers of phenols, examples of which are shown in Figure 6.3. The name is derived from “calix”, which is Greek for vase, and “arenes” because of the aromatic moieties present in the macromolecule. To name specific calixarenes, a prefix is added to indicate how the macromolecule has been modified; the digit between “calix” and “arene” refers to the number of benzene rings in the macromolecule. These molecular vases have been derivatized in many ways to achieve desired physical and chemical properties. For example, many metal complexes have been attached on the lower rim (where the phenolic OH is located) to achieve catalysts for the Wacker oxidation of olefins [127]. The upper rim (position opposite [*para*-] the –OH), on the other hand, has been derivatized to improve solubility in water and prevent conformational changes [128].

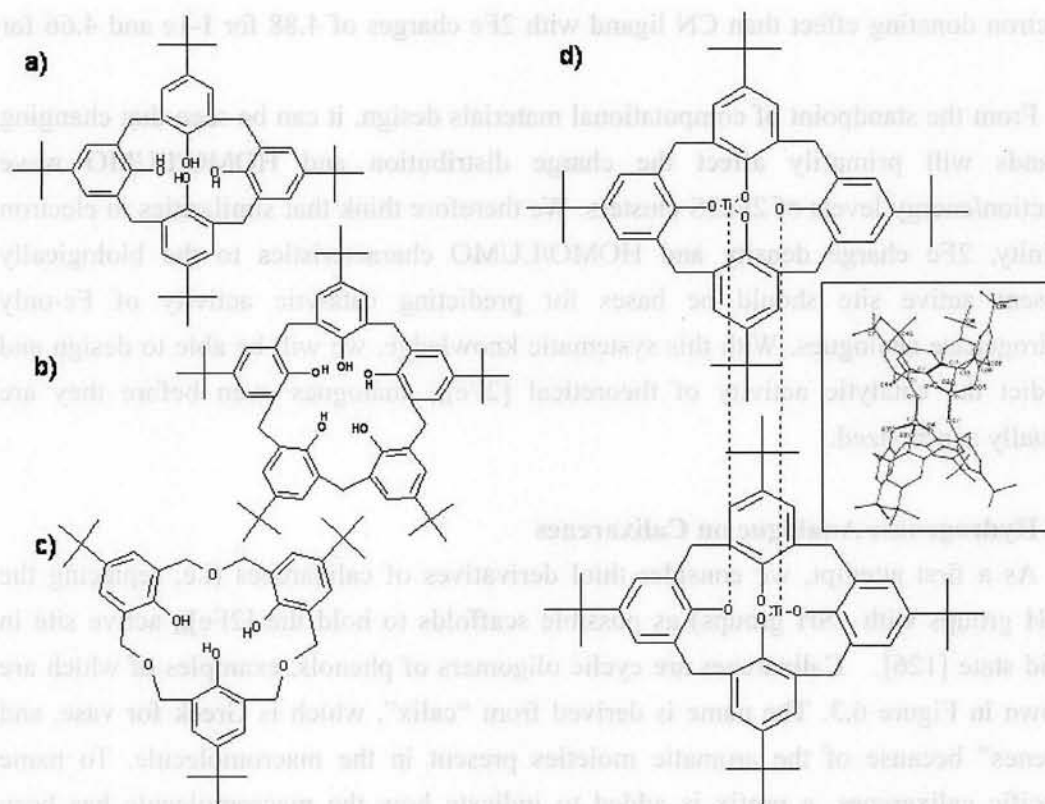


Figure 6.3. Examples of calixarenes. (a) p-tert-butylcalix[4]arene [129] (b) 25,26,27,28,29-pentahydroxycalix[5]arene [130] (c) hexahomotrioxacalix[3]arene [128] (d) titanium(IV) p-tert-butylcalix[4]arene complex [131].

As a testament of its metal-holding ability, a number of patents have been issued involving the use of calixarenes as ionophores. Izatt et. al. was awarded a patent for a process that uses a calixarenes to recover cesium from radioactive waste [132]. The Hitachi Chemical Co. were issued a patent for preparing calixarenes and using them as absorbents of heavy metals [133] Shinkai et al., have been issued a patent for the use of a calixarene to trap uranium as UO_2^{2+} in sea water. The resin is stated to absorb 108 $\mu\text{gU}/0.1\text{g}$ in 7 days at a flow rate of 20 ml/min. [134].

We aim to mimic the $[\text{2Fe}]_{\text{H}}$ sub-site of hydrogenase by first replacing the $-\text{OH}$ groups of calixarenes with $-\text{SH}$ groups [126]. More importantly, however, the sulfur atoms have to be at certain positions on a calixarene that resembles the hydrogenase di-iron site. While calixarenes may vary in conformations and sizes, finding the right scaffold remained challenging. We employ various steps in materials design, which can be summarized into the following steps:

Step 1. We perform DFT calculations on $[\text{2Fe}]_{\text{H}}$ subcluster analogues

[(PDT)Fe₂(CO)₆] (a) and [(PDT)Fe₂(CO)₄(CN)₂]²⁻ (b) and confirmed modelling parameters by comparing our results (Table 6.3) versus IR data obtained by experiment [56, 135-136] and previous DFT calculations [57]. We then performed DFT calculations on a hydrogenase analogue similar to what we expect to obtain from our design (Figure 6.4) as implemented in Gaussian03 [104]. The system carries a charge of -1 and multiplicity of 1. The basis set and exchange/correlation functionals were 6-31+G(d,p) and B3LYP respectively. The charge was chosen because [2Fe]_H analogues generally contain Fe(I)Fe(I) centers during synthesis. The Fe-Fe optimized distance is 2.51 Å. Those for Fe-S1 and Fe-S2 are between 2.36-2.38 Å, for Fe-S3 is 2.32 Å, and for S1-S2 is 3.37 Å.

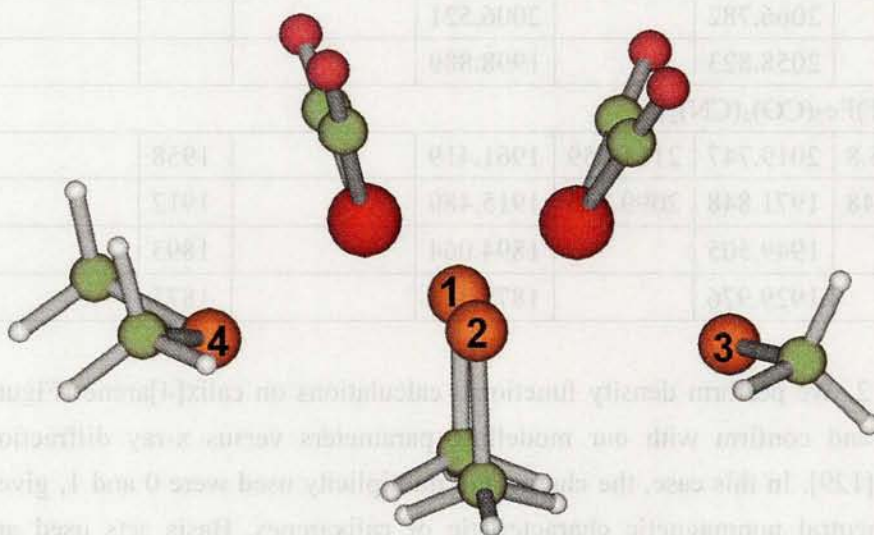


Figure 6.4. [2Fe]_H subcluster analogue similar to what we expect obtain to from our design. Sulfurs are numbered for later (Table 6.4) reference.

Table 6.3. Comparison of IR Frequencies (cm^{-1}) of $[\text{2Fe}]_{\text{H}}$ subcluster analogues $[(\text{PDT})\text{Fe}_2(\text{CO})_6]$ (a) and $[(\text{PDT})\text{Fe}_2(\text{CO})_4(\text{CN})_2]^{2-}$ (b) between our calculated/predicted results [ν_i (predicted) = $24.684 + 0.95189 \nu_i(\text{calcd})$] versus those predicted by a previous DFT study [57] and by experiments [56, 135-136]

This study				Obtained by Cao and Hall DFT calcs.		Experimental
Calculated		predicted		Predicted		
CN	CO	CN	CO	CN	CO	
a) $[(\text{PDT})\text{Fe}_2(\text{CO})_6]$						
	2141.499		2078.167		2069	2072
	2092.787		2031.458		2020	2033
	2084.799		2023.798		2017	2033
	2068.294		2007.971		2005	1993
	2066.782		2006.521			
	2058.823		1998.889			
b) $[(\text{PDT})\text{Fe}_2(\text{CO})_4(\text{CN})_2]^{2-}$						
2175.8	2019.747	2111.059	1961.419		1958	1962
2163.48	1971.848	2099.245	1915.489		1912	1921
	1949.505		1894.064		1893	1883
	1929.976		1875.338		1875	

Step 2. We perform density functional calculations on calix[4]arene (Figure 6.5) and confirm with our modelling parameters versus x-ray diffraction data [129]. In this case, the charge and multiplicity used were 0 and 1, given the neutral nonmagnetic characteristic of calixarenes. Basis sets used are LanL2DZ for C and H of calixarene, and 6-31+G* for O and 6-311**G++ for the four OH hydrogen atoms. 6-31+G* was used for oxygen to be consistent with the basis set used for S in step 1. Bigger basis sets for the -OH hydrogen atoms are necessary to account for the hydrogen bonding between the H and a rather far neighboring O. The B3LYP exchange and correlation functionals were used. The $\text{C}_{\Phi}\text{-C}_{\Phi}$ (C_{Φ} is benzene ring carbon) distance is 1.41\AA , $\text{C}_{\Phi}\text{-C}_{\text{CH}_2}$ (C_{CH_2} is methyl carbon) distance is 1.53\AA , $\text{C}_{\Phi}\text{-H}$ distance is 1.09\AA and the $\text{C}_{\text{CH}_2}\text{-H}$ distance is 1.10\AA . All these are typical bond lengths as expected. But more importantly, the O-O distance is 2.65\AA , which is very close to the experimentally reported 2.67\AA [129].

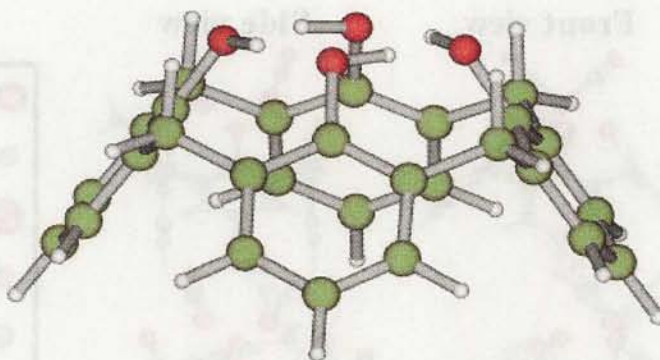


Figure 6.5. Calix[4]arene.

Step 3. We use molecular modelling kits (from HGS Maruzen) to roughly determine the orientations of calixarenes that will likely hold the di-iron site as shown in Figure 6.6. The bond lengths in the models are at a 2.5 cm:1 Å ratio versus the molecule. Drilled polygons were used to represent atoms; the drilled holes were precisely situated to reproduce angles of atomic hybridization. Bond lengths and the geometry of our $[2\text{Fe}]_{\text{H}}$ site are based on our DFT calculations. The S-S bond distance, for example, was custom cut to correspond to 3.37 Å.

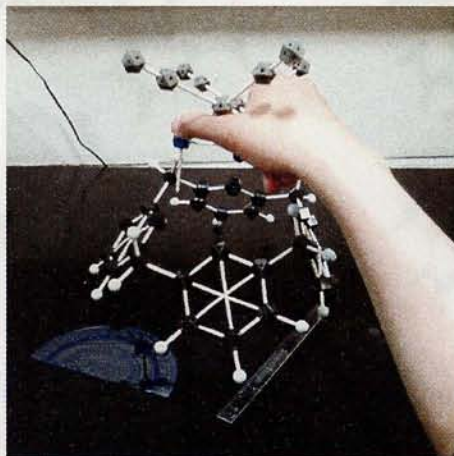


Figure 6.6. Estimating the fit of $[2\text{Fe}]_{\text{H}}$ on calixarenes.

Step 4. We model the $[2\text{Fe}]_{\text{H}}$ active site on calixarenes from step 3 *in silico* and perform density functional calculations to determine the optimized geometry of these compounds. We have performed geometry relaxation for a di-iron cluster on calix[4]arene, calix[5]arene and oxacalix[3]arene. We did additional calculations on calix[3]arene by replacing the oxa ($-\text{CH}_2\text{-O-CH}_2-$) linkage with thia ($-\text{CH}_2\text{-S-CH}_2-$) and propyl $(\text{CH}_2)_3$ linkages. The results are shown in Figure 6.7 below and tabulated in Table 6.4.

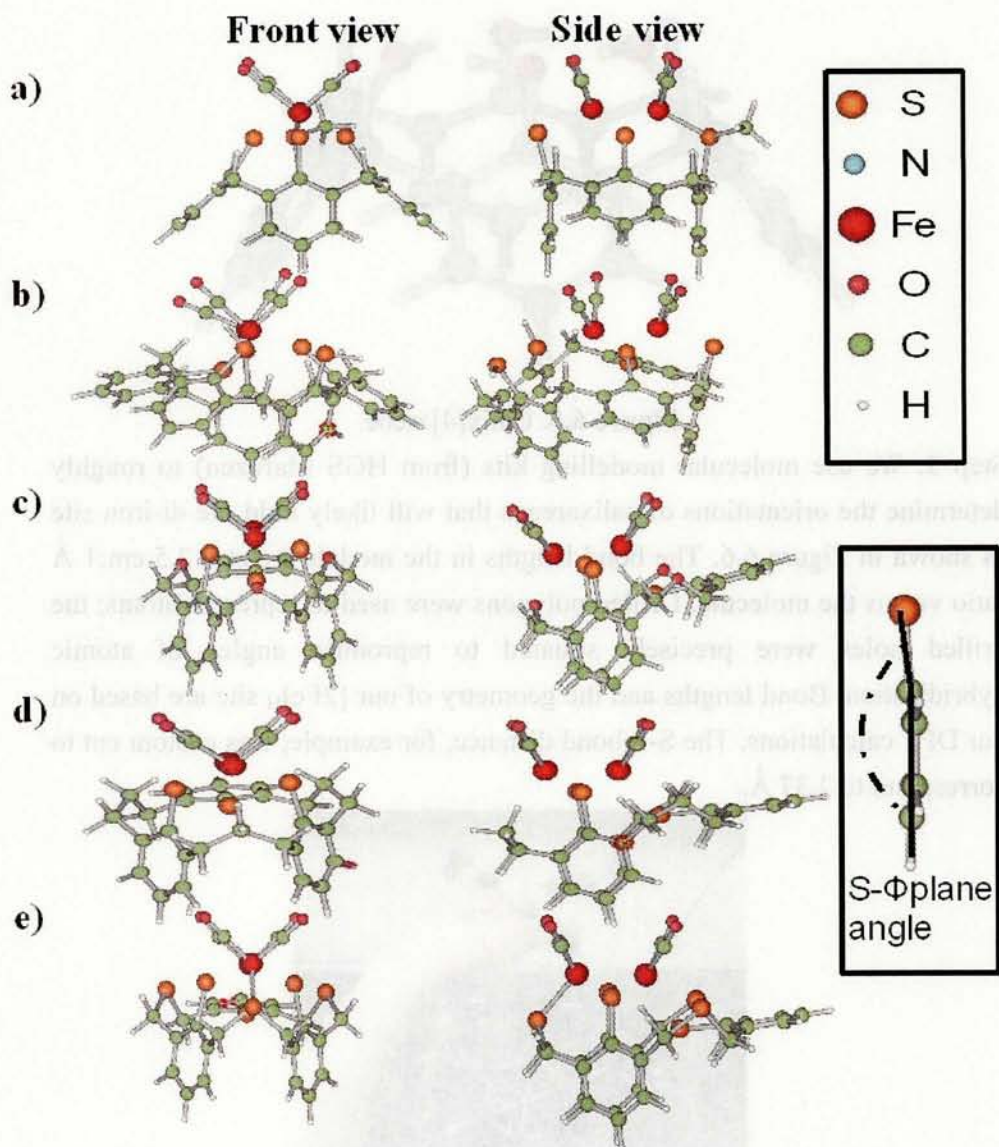


Figure 6.7. Figure 5. Optimized geometry of a $[2\text{Fe}]_{\text{H}}$ subcluster on a) calix[4]arene, b) calix[5]arene, calix[3]arenes with ester ($-\text{CH}_2\text{-O-CH}_2-$) c) , propyl ($-\text{CH}_2\text{-CH}_2\text{-CH}_2-$) d) and sulfide ($-\text{CH}_2\text{-S-CH}_2-$) e) linkages. The upper inset shows the legend of the atoms. The lower inset shows the S- Φ plane angle between a sulfur atom and its benzene ring.

Table 6.4. Optimized geometry of [2Fe]_H subclusters on calixarenes. Bond lengths are given in Angstroms (Å) and angles in degree (°). Sulfurs are labeled as shown in Figure 6.4.

	Calix[4]arene	Calix[5]arene	Calix[3]arene		
			oxa	propyl	thia
Fe-Fe distance	2.52 Å	2.51 Å	2.73 Å	2.50 Å	2.61 Å
Fe-S(1&2)	2.39, 2.42 Å	2.34, 2.36 Å	2.53 Å	2.37, 2.44 Å	2.35, 2.39 Å
Fe-S(3)	2.30 Å	2.33 Å	2.33 Å	2.36 Å	2.39 Å
Fe-S(4)	2.27 Å	2.39 Å			
Fe-S(5)		4.63 Å			
S(1)-S(2)	3.50 Å	3.18 Å	3.60 Å	3.67 Å	3.64 Å
S(1)-Φplane	164.3°	174.8°	178.8°	176.0°	174.4°
S(2)-Φplane	164.7°	167.1°	178.8°	176.0°	174.4°
S(3)-Φplane	168.4°	178.4°	178.0°	178.2°	176.9°
S(4)-Φplane	172.0°	177.9°			

As can be seen from the figures and the tables above, the sulfurs are pushed out of the benzene planes to accommodate the di-iron center. (The angle between a sulfur atom and its benzene plane, S-Φplane [defined in the lower inset of Figure 6.7], should ideally be 180°.) Consequently, we have to know how much strain is caused by such sulfur arrangements.

So lastly, in step 5, we removed the active site from our calixarene scaffold and re-optimized the geometry (of the scaffold only without the active site). The energy difference between the initial geometry and the relaxed geometry ($E_{\text{strain}} = E_{\text{initial geometry without active site}} - E_{\text{relax geometry without active site}}$) gives us a good idea of the strain caused by the [2Fe]_H group on the calixarene scaffold. The strain caused by [2Fe]_H group are equivalent to E_{strain} values of 0.92 eV for Calix[4]arene, 0.65 eV for Calix[5]arene and 0.73 eV for oxacalix[3]arene. For reference, we also calculated the E_{strain} for DTMA, which turned out to be 0.06 eV. Replacing -CH₂-O-CH₂- of oxacalixarene with -CH₂-S-CH₂- (i.e., thiacalix[3]arene) and (CH₂)₃ increases the strain to 1.19 eV and 0.98 eV respectively.

Our calculations has shown that calix[5]arene is the most viable macrocycle to hold the di-iron site based on an E_{strain} of 0.65 eV. Our calculations also show that the crucial hydrogenase active site is maintained in this material: having an Fe-Fe bond (2.51 Å)

and anti-bond at the HOMO and LUMO respectively (Figure 6.8); and the bonding orbitals on the Fe centers connected to the sulfur of the electron chain (in our case, S3) at the HOMO. Although oxacalix[3]arene may appear to the next best alternative based on E_{strain} (0.73 eV), the Fe-Fe bond is broken in this configuration (Fe-Fe distance is 2.73 Å).

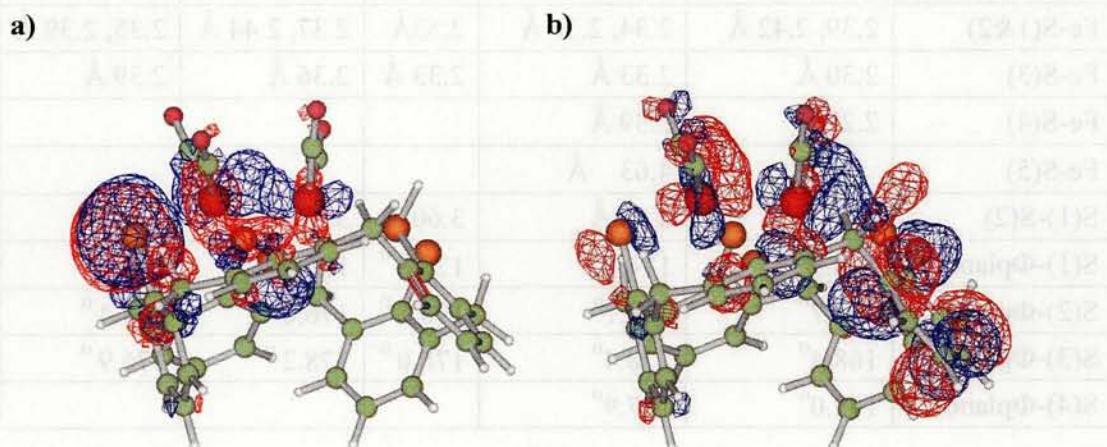


Figure 6.8. HOMO (a) and LUMO (b) of the di-iron cluster on calix[5]arene thiol.

Chapter Seven

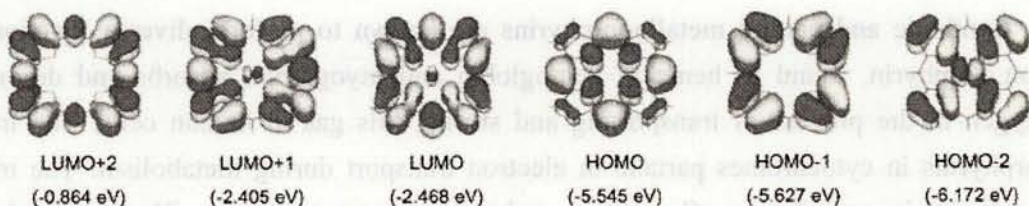
Design of Novel Heme-based Catalyst for ORR

Synthetic and natural metalloporphyrins are known to perform diverse functions. Iron porphyrin, found as heme in hemoglobin and myoglobin, adsorbs and desorbs oxygen in the process of transporting and storing this gas in human cells. The iron porphyrins in cytochromes partake in electron transport during metabolism. The iron porphyrin in cytochrome C oxidase reduces oxygen to water. The magnesium porphyrins in chlorophylls trap and use solar energy to synthesize plant tissues from carbon dioxide and water. Synthetic platinum porphyrins are being used as oxygen sensors due to the fluorescence quenching effect of this gas. Synthetic metalloporphyrin compounds have also demonstrated potential as oxygen reduction catalysts [89-91].

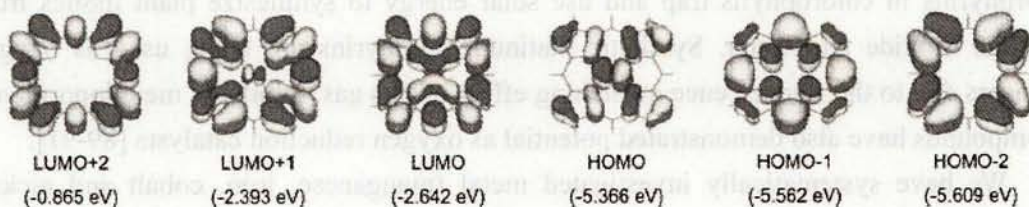
We have systematically investigated metal (manganese, iron, cobalt and nickel) porphyrin systems for oxygen reduction by density-functional in light of PEFC applications [78]. We investigated the effect of these metal porphyrins on the O–O bond strength upon adsorption. It was found that O₂ bond weakening/dissociation capability of a certain metalloporphyrin depends on whether the LUMO–HOMO levels involve the corresponding metal centers, which in turn depends on the d-orbital occupancies of the metals. The contributions from the d-electrons of the metal centers to the LUMO–HOMO levels drop as their d-orbital occupancies increase, which can be simply explained as the periodic properties of these elements. For iron and manganese porphyrin, the d electrons of the metal centers contribute to the LUMO and HOMO (Figures 7.1a and 7.1b). For nickel and cobalt porphyrin (Figures 7.1c and 7.1d), on the other hand, the d-electrons of the metal centers contribute only to the LUMO(~LUMO+1); their d-electrons make no contribution to the HOMO levels, and their HOMO levels only possess porphyrin characters. The catalytic activity of these metal porphyrins in the order of best to worst was found to be: iron, manganese, nickel, cobalt.

a)

α electrons of FeP

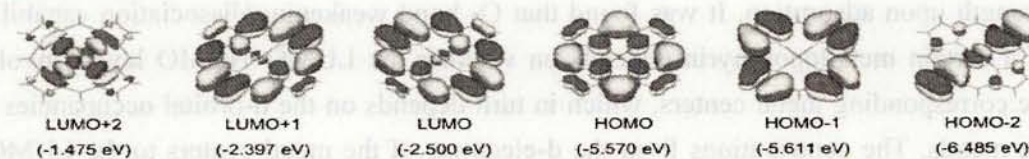


β electrons of FeP

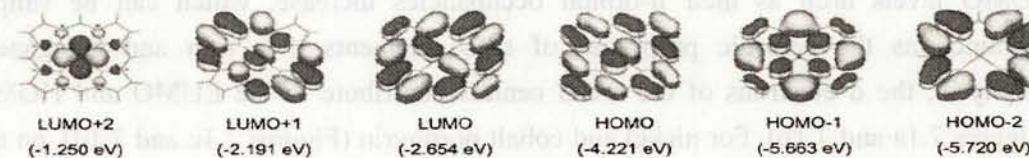


b)

α electrons of MnP

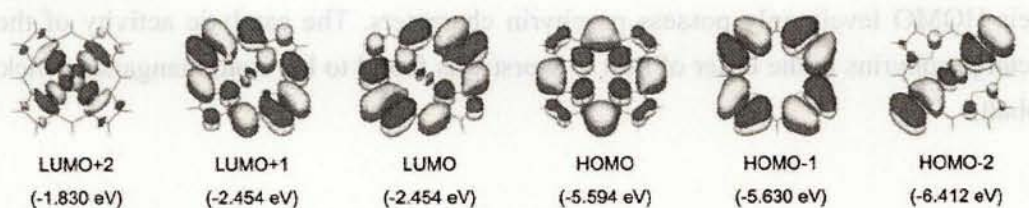


β electrons of MnP

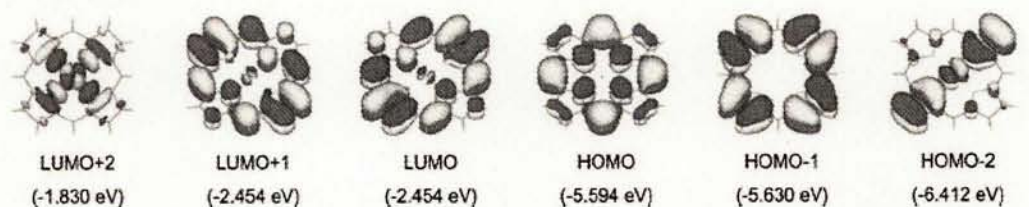


c)

α electrons of NiP

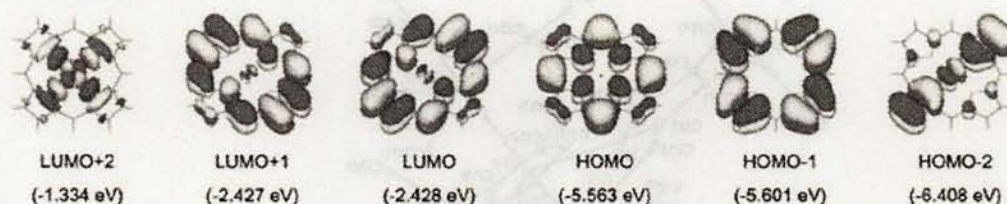


β electrons of NiP



d)

α electrons of CoP



β electrons of CoP

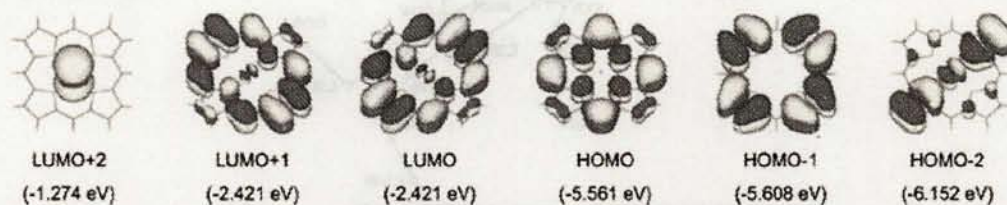


Figure 7.1. Schematic representations of the LUMO, LUMO+1 and LUMO+2; and HOMO, HOMO-1 and HOMO-2 of the α and β electrons of the iron-, manganese-, nickel- and cobalt-porphyrin. Their orbital energies are given in eV.

7.1 Depositing Pt on SnPor.

Among the metalloporphyrins, perhaps one of the most overlooked is tin (II) porphyrin (SnPor). It is possibly because SnPor alone is known not to interact with ligands, such as water, and slowly oxidizes in the presence of oxygen [137-138]. Experimental studies have shown that tin (II) porphyrin (SnPor) can deposit metals—such as iron (Fe), magnesium (Mg), rhenium (Re) and cobalt (Co)—on its surface as shown in Figure 7.2. Compared to the metal-porphyrins we studied in the past [78], these metals bonded on SnPor can be neutral (the metals in metal-porphyrins are cations). The Mg and Co deposited on SnPor can further bond with metals such as mercury (Hg), manganese (Mn), cadmium (Cd), cobalt (Co) and zinc (Zn) forming a wire. Many of these compounds have been studied for their spectral, magnetic and electrochemical properties. Their structures have been confirmed by X-ray diffraction [139-144]. Studies have also demonstrated photocatalytic properties of tin porphyrins with Pt ions in solution. The reactions catalyzed include the reduction of protons into hydrogen gas with ascorbic acid as electron donors and the self-assembly of Pt nanoparticles [145-147]. However, depositing platinum as individual atoms on germanium, tin or lead porphyrins has not been reported.

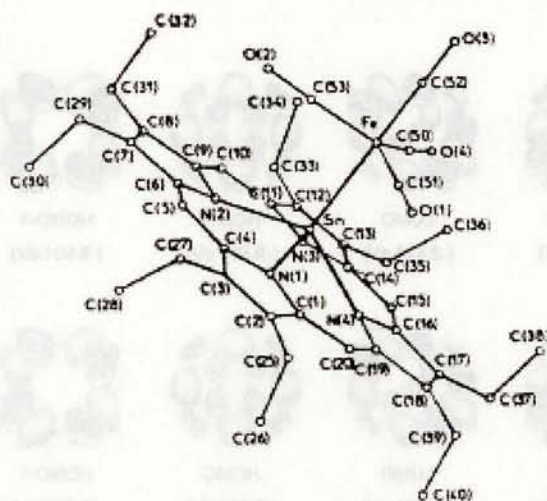


Figure 1. Single-crystal X-ray structure of (OEP)SnFe(CO)₄.

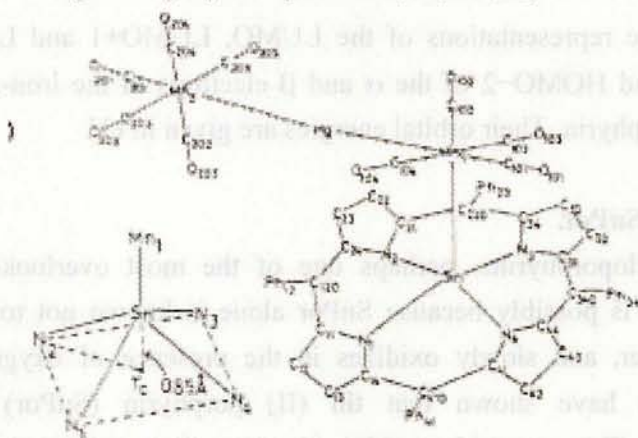


Figure 7.2. X-ray diffraction data of metals deposited on SnPor taken from Ref. [139] and [140].

We consider depositing Pt directly on SnPor surface as a way to minimize Pt load in catalysts [148]. We modeled SnPor and SnPor–Pt and performed density functional calculations with GAUSSIAN 03 [104] as shown in Figure 7.3. We used the LANL2DZ basis set and the three-parameter Becke/Lee–Yang–Parr (B3LYP) exchange-correlation functionals. It should be noted that both Sn(II) and Sn(IV) can react with porphyrins to form SnPor (neutral) and SnPor²⁺, respectively. However, experimental studies show that transition metals can deposit on SnPor. Also, our calculations show that the SnPor²⁺–Pt has its Sn ion out of the porphyrin plane similar to that of SnPor–Pt and is energetically less stable than SnPor–Pt. Therefore, SnPor²⁺–Pt will likely be neutralized by two electrons to SnPor–Pt anyway before it accepts another electron to donate to a ligand during reduction reaction.

We consider SnPor and SnPor–Pt with spin multiplicities of 1, 3, 5, and 7 to determine the ground state of both compounds. We fully relaxed the geometry at each spin state. Using the same computational conditions mentioned above, we also calculated the energy and optimized geometry of SnPor–Pt with a negative one (-1) charge. We repeated calculations for SnPor and SnPor–Pt to confirm the Mulliken charge distribution of using the SDD basis set. The Mulliken charge distribution obtained was similar (difference of <0.1). However, LANL2DZ yielded a slightly better geometric agreement with X-ray diffraction data for SnPor, and so we report the data therefrom.

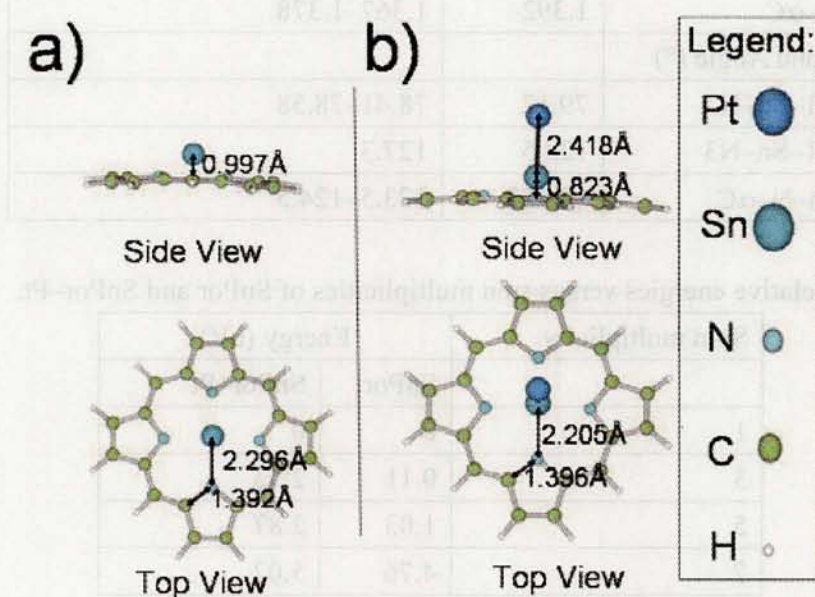


Figure 7.3. Optimized geometry of: (a) SnPor and (b) SnPor–Pt.

We first computed for the ground state of SnPor and compared our results with the geometry obtained experimentally by X-ray diffraction [138] to confirm the suitability of our selected computational parameters. Our results are well within the expected accuracy of DFT calculations as shown in Table 7.1. N plane refers to the average of all possible planes defined three-atom combinations of the four nitrogen atoms. α C refers to the carbons directly bonded to nitrogen. N1-N2 refers to nitrogens that are beside each other while N1-N3 refers to nitrogens that are opposite each other.

Our calculations indicate that the ground state is a singlet (Table 7.2), which is consistent with its observed diamagnetism. The geometry is non-planar as shown in Figure 7.3a. Sn lies 0.997 Å above the plane of the porphyrin. This has been attributed to the huge atomic radius of Sn(II), which discourages it from fitting into the relatively small porphyrin ring center.

Table 7.1. Calculated versus experimental values of important geometric parameters of SnPor. N plane refers to the average of all possible planes defined three-atom combinations of the four nitrogen atoms. α C refers to the carbons directly bonded to nitrogen. N1-N2 refers to nitrogens that are beside each other while N1-N3 refers to nitrogens that are opposite each other.

	Calculated	Experimental [138]
Bondlength (Å)		
Sn–N	2.296	2.276–2.286
Sn–N Plane	0.997	1.018
N– α C	1.392	1.367–1.378
Bond Angle (°)		
N1–Sn–N2	79.12	78.41–78.58
N1–Sn–N3	128.5	127.3
Sn–N– α C	124.82	123.5–124.5

Table 7.2. Relative energies versus spin multiplicities of SnPor and SnPor–Pt.

Spin multiplicity	Energy (eV)	
	SnPor	SnPor–Pt
1	0	0
3	0.11	2.53
5	1.03	2.87
7	4.76	5.02

We proceeded with calculating the interaction between SnPor and Pt. The relaxed geometry is shown in Figure 7.3b. The bond distance between Pt and Sn is 2.418 Å. Our calculations gave a binding energy of 3.13 eV. This indicates that SnPor–Pt is very stable. Figure 7.4a illustrates the bonding orbitals between the Pt and SnPor. The Sn sp_z components of these orbitals donate electrons to partly filled orbitals of Pt; this leads to the spin relaxation of Pt into the singlet state. In other words, SnPor acts like a ligand bonding to Pt. Of note, the molecular orbital 86 of SnPor–Pt in Figure 7.4a corresponds to the HOMO of SnPor bonding with d_z^2 sp atomic orbital components of Pt. This suggests that the bond between Pt and M is more of a metal-ligand interaction rather than a metal-metal bond. We also see interaction between the p_z orbitals of N from the porphyrin and the d_z^2 orbital of platinum. More importantly, upon comparing the energies of orbitals in Figures 7.4a, 7.4b and 7.4c, it can be seen that the bonding orbitals (Figure 7.4c) are much lower in energy than the frontier orbitals. This indicates

that electrons in these bonding states will not be involved in chemical reactions that will result in the breaking of the Pt-SnPor bond, implying that Pt will deposit tightly on SnPor during chemical reactions.

The resulting compound yields a very interesting electronic structure with more than 92% of the total electron density delocalized in the porphyrin ring, yet all the HOMO and near-HOMO electrons (frontier electrons) correspond primarily to the valence d-electrons of Pt as shown in Figure 7.4c. The Mulliken charge analysis shows that the Pt is partially negative (Table 7.3).

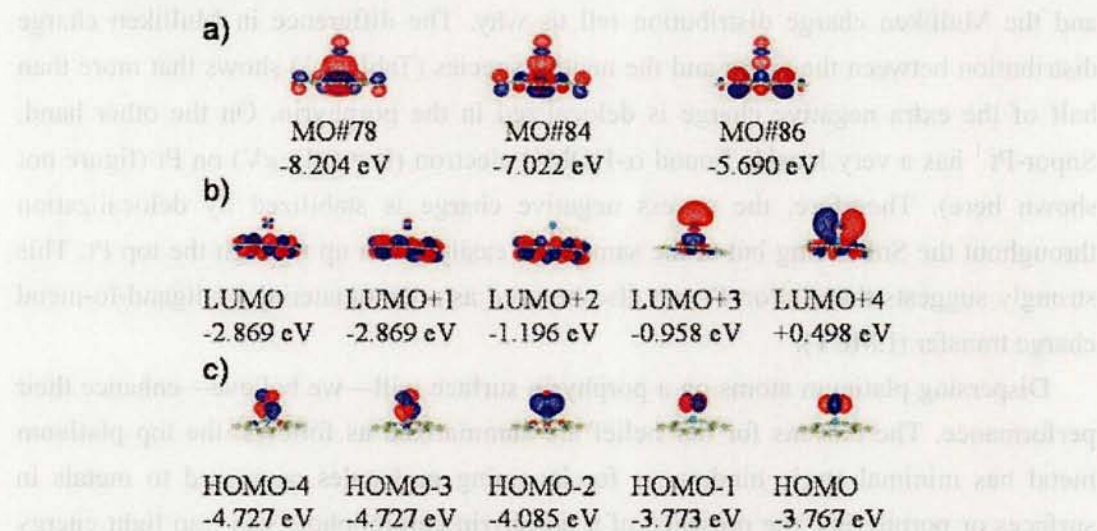


Figure 7.4. Important molecular orbitals of SnPor-Pt: (a) molecular orbitals showing bonding between the SnPor and Pt, (b) LUMO to LUMO+4 levels, and (c) HOMO-4 to HOMO levels.

Table 7.3. Mulliken charge distribution of neutral SnPor-Pt, SnPor-Pt⁻¹ anion and their charge difference.

	SnPor-Pt	SnPor-Pt ⁻¹	Diff [SnPor-Pt ⁻¹ -SnPor-Pt]
Por	-0.78	-1.32	-0.54
Sn	1.41	1.30	-0.11
Pt	-0.63	-0.98	-0.35
Total	0.00	-1.00	-1.00

The low electron density near Pt, partial negative charge of Pt, and the high Pt-character near and at HOMO levels all indicate that this Pt is the preferred site for bonding with an electrophile for reduction reactions. A Pt with such electronic characteristics will also likely induce a dipole moment on non-polar molecules for

reduction. The LUMO, on the other hand, still possess significant Pt d-orbital characteristics comparable to the α - and β -LUMO of iron porphyrin (Figure 7.1), further suggesting ability to interact with oxygen for catalytic reduction.

We also calculated the electron affinity ($EA = [E(\text{electronic, optimized neutral}) + E(\text{zero-point vibration, neutral})] - [E(\text{electronic, optimized anion}) + E(\text{zero-point vibration, anion})]$) of SnPor–Pt, which yielded value of 0.13 eV. This is much lower than the EA of Pt metal. A near-zero EA indicates that SnPor–Pt neither needs much energy to buffer nor give up an extra electron. A closer look into the molecular orbitals and the Mulliken charge distribution tell us why. The difference in Mulliken charge distribution between the anion and the neutral species (Table 7.3) shows that more than half of the extra negative charge is delocalized in the porphyrin. On the other hand, Snpor–Pt⁻¹ has a very loosely bound α -HOMO electron ($E = 0.12$ eV) on Pt (figure not shown here). Therefore, the excess negative charge is stabilized by delocalization throughout the SnPor ring but at the same time easily given up through the top Pt. This strongly suggests that SnPor–Pt can also be used as a nanomaterial for ligand-to-metal charge transfer (LMCT).

Dispersing platinum atoms on a porphyrin surface will—we believe—enhance their performance. The reasons for our belief are summarized as follows: the top platinum metal has minimal steric hindrances for incoming molecules compared to metals in surfaces or porphyrins; the presence of a porphyrin chromophore can trap light energy possibly assisting the catalytic processes; the perturbation on the electronic structure of Pt by the SnPor, as our calculations indicate, enhances its catalytic properties by the inducing partial negative charge on Pt, the lowering electron density at Pt and the localization of frontier (HOMO and near-HOMO) electrons on Pt. Another unique electronic property of SnPor–Pt is that this compound has an EA near zero. SnPor stabilizes the extra negative charge while a very loose HOMO electron is easily given up by Pt.

7.2 Comparing interaction of Pt on SnPor with GePor and PbPor.

Since experimental studies have shown that GePor can also deposit metals [142], we continued our research by comparing the interaction of Pt with all group 4A metal porphyrins [149]—i.e., GePor, SnPor, and PbPor—as shown in Figure 7.5. Following our previous study [138], we show the results of our calculations for GePor–Pt and PbPor–Pt in comparison to SnPor–Pt. Likewise, we performed density functional calculations with Gaussian03 [104] using the LanL2DZ basis set and the three-parameter Becke/Lee-Yang-Parr (B3LYP) exchange-correlation functionals.

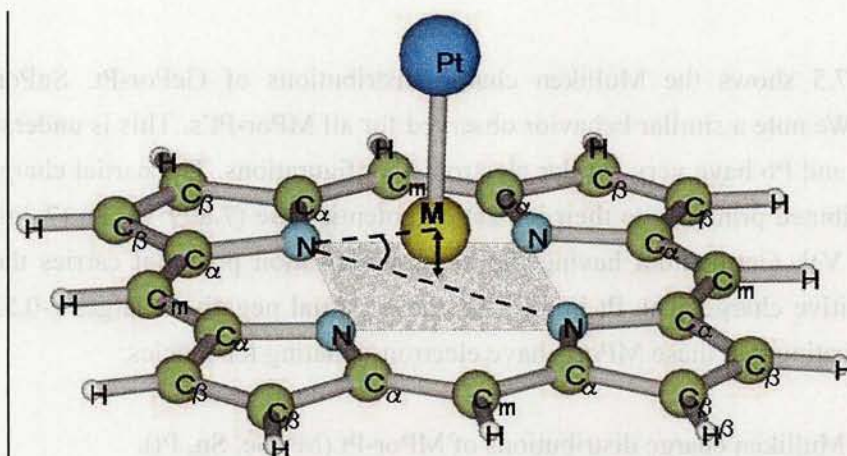


Figure 7.5. Geometry of MPor-Pt, where M=Ge, Sn and Pb.

We fully optimized the geometries of all compounds. The relaxed geometries of MPor-Pt (M=Ge, Sn and Pb) are summarized in table 7.4. The geometric parameters are as shown in Figure 7.5. The N plane (the mean plane formed by the four N's of porphyrin) is shown as a shaded surface; the M-N plane distance is shown as a double-headed arrow; the angle between M and the N plane is shown as dashed lines. The bond distances between M and the N plane are accounted for by differences in atomic radii of the metals (Ge=1.52 Å, Sn=1.72 Å, Pb=1.81 Å). The trend in M-Pt bond distance can likewise be explained by differences in the atomic radii of M. As expected, the geometries of the porphyrin rings are not significantly different between the three MPor-Pt's.

We confirmed that the ground states of these compounds were singlets. Our calculations gave energies of 3.13 eV for both the binding Pt on GePor and on SnPor, but only 1.99 eV for PbPor.

Table 7.4. Calculated geometric parameters of MPor-Pt (M=Ge, Sn, Pt).

	GePor-Pt	SnPor-Pt	PbPor-Pt
Distance (Å):			
N plane-M	0.679	0.823	0.947
N-M	2.113	2.205	2.278
M-Pt	2.283	2.418	2.472
N-C α	1.399	1.396	1.393
C α -C β	1.447	1.451	1.455
C α -C m	1.390	1.398	1.403
Angle (°):			
M-N plane	18.74	21.92	24.56

Table 7.5 shows the Mulliken charge distributions of GePor-Pt, SnPor-Pt and PbPor-Pt. We note a similar behavior observed for all MPor-Pt's. This is understandable as Ge, Sn, and Pb have very similar electronic configurations. The partial charges on M can be attributed primarily to their ionization potential [Ge (7.899 V), Sn (7.344 V) and Pb (7.416 V)]. Germanium having the highest ionization potential carries the lowest partial positive charge. The Pt in all cases have partial negative charges (-0.53, -0.62, -0.50) indicating that these MPor's have electron-donating tendencies.

Table 7.5. Mulliken charge distributions of MPor-Pt (M=Ge, Sn, Pt).

	GePor-Pt	SnPor-Pt	PbPor-Pt
Pt	-0.53	-0.62	-0.50
M	1.22	1.41	1.28
N	-0.51	-0.55	-0.49
C α	0.44	0.44	0.41
C β	-0.37	-0.36	-0.36
C γ	-0.55	-0.54	-0.54

The near HOMO and near LUMO states are shown in Figures 7.6 and 7.7. We see here that the frontier orbitals are quite similar for all Mpor-Pt's. Valence Pt d-orbital characteristics dominate HOMO and HOMO-1.

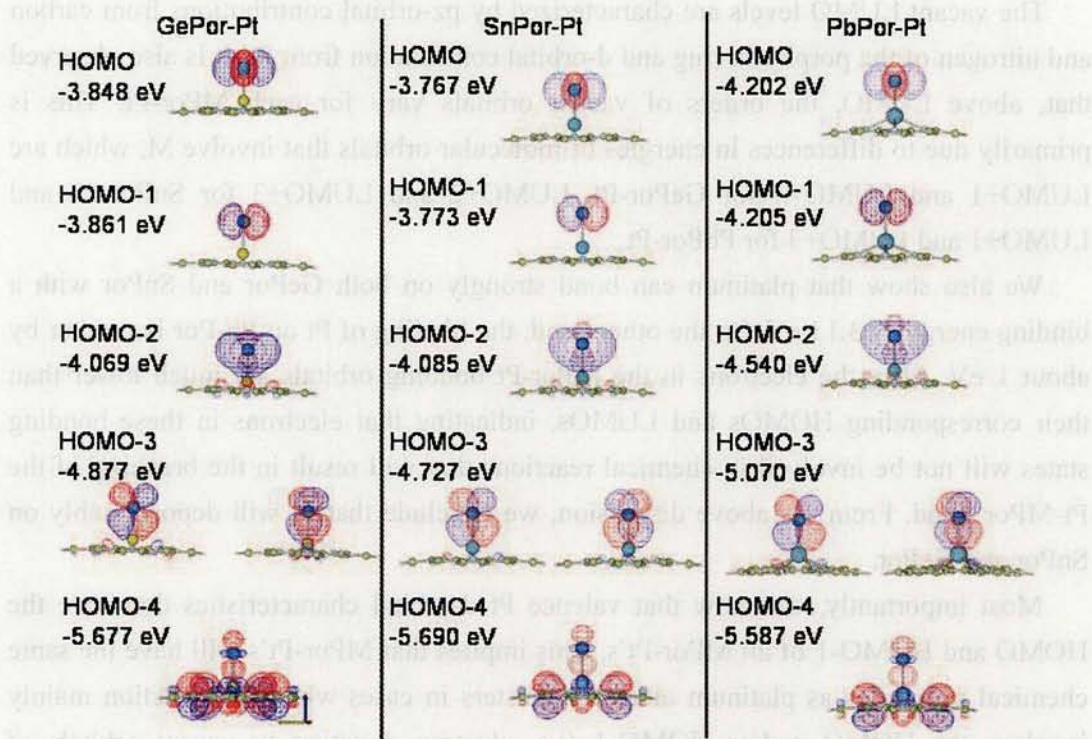


Figure 7.6. HOMO and Near-HOMO levels of MPor-Pt (where M=Sn, Ge and Pb).

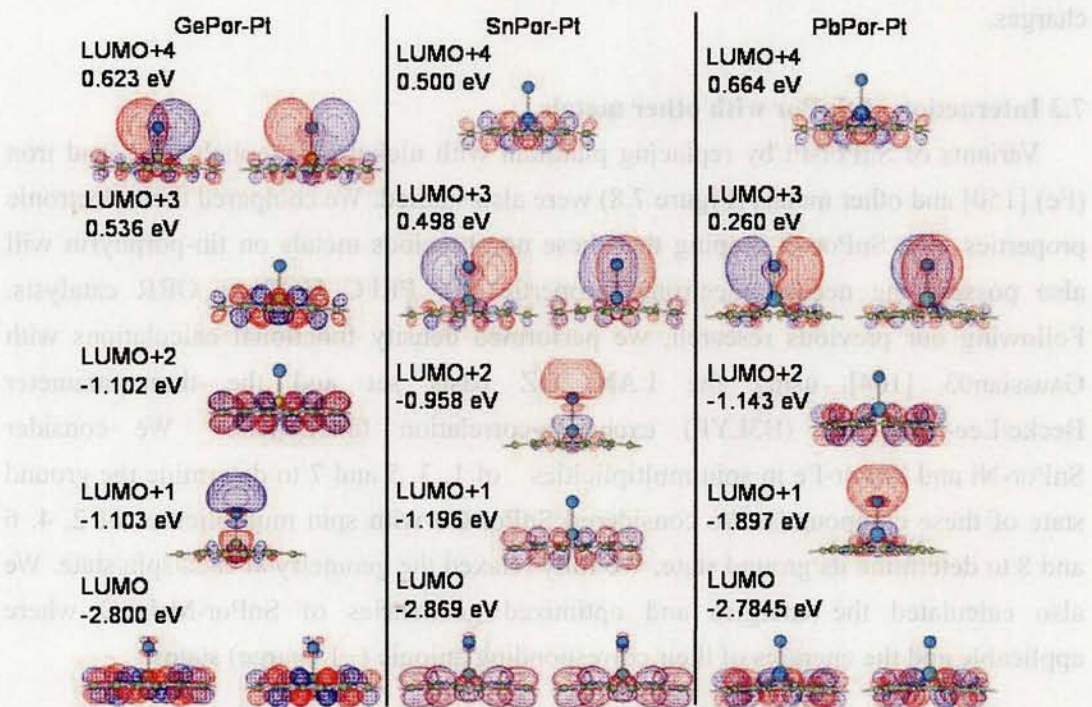


Figure 7.7. LUMO and Near-LUMO levels of MPor-Pt (where M=Sn, Ge and Pb).

The vacant LUMO levels are characterized by pz-orbital contributions from carbon and nitrogen of the porphyrin ring and d-orbital contribution from Pt. It is also observed that, above LUMO, the orders of vacant orbitals vary for each MPor-Pt. This is primarily due to differences in energies of molecular orbitals that involve M, which are LUMO+1 and LUMO+4 for GePor-Pt, LUMO+2 and LUMO+3 for SnPor-Pt, and LUMO+1 and LUMO+3 for PbPor-Pt.

We also show that platinum can bond strongly on both GePor and SnPor with a binding energy of 3.13 eV. On the other hand, the binding of Pt on Pb-Por is weaker by about 1 eV. Also, the electrons in the MPor-Pt bonding orbitals are much lower than their corresponding HOMOs and LUMOs, indicating that electrons in these bonding states will not be involved in chemical reactions that will result in the breaking of the Pt-MPor bond. From the above discussion, we conclude that Pt will deposit stably on SnPor and GePor.

Most importantly, we show that valence Pt d-orbital characteristics dominate the HOMO and HOMO-1 of all MPor-Pt's. This implies that MPor-Pt's will have the same chemical properties as platinum atoms or clusters in cases where the reaction mainly involves the HOMO and/or HOMO-1 (i.e. electron donation to vacant orbitals of adsorbates), of which the oxygen reduction reaction in fuel cells is an example. This argument is further reinforced by the fact that Pt atoms in MPor-Pt have partial negative charges.

7.3 Interaction of SnPor with other metals.

Variants of SnPor-Pt by replacing platinum with nickel (Ni), cobalt (Co), and iron (Fe) [150] and other metals (Figure 7.8) were also studied. We compared their electronic properties with SnPor-Pt, hoping that these non-precious metals on tin-porphyrin will also possess the needed electronic properties for PEFC HOR or ORR catalysts. Following our previous research, we performed density functional calculations with Gaussian03 [104] using the LANL2DZ basis set and the three-parameter Becke/Lee-Yang-Parr (B3LYP) exchange-correlation functionals. We consider SnPor-Ni and SnPor-Fe in spin multiplicities of 1, 3, 5 and 7 to determine the ground state of these compounds. We considered SnPor-Co with spin multiplicities of 2, 4, 6 and 8 to determine its ground state. We fully relaxed the geometry at each spin state. We also calculated the energies and optimized geometries of SnPor-M•H₂O where applicable and the energies of their corresponding anionic (−1 charge) states.

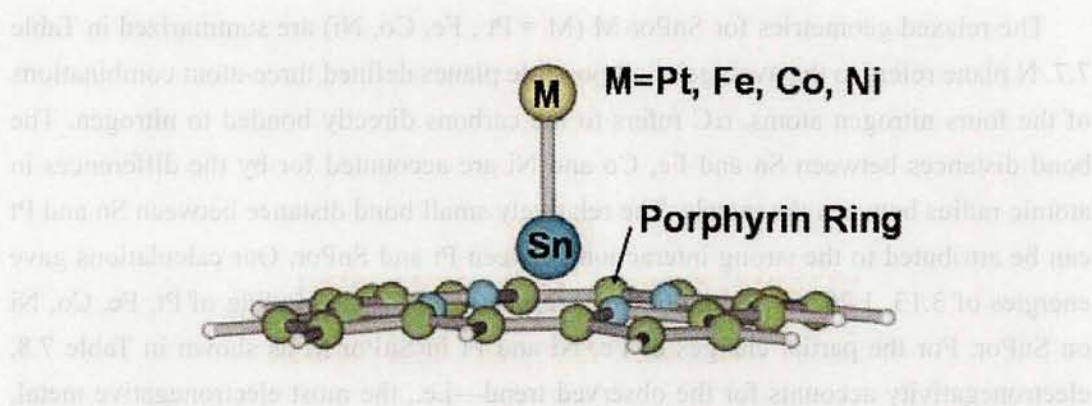


Figure 7.8. Geometry of SnPor-M, where M=Pt, Fe, Co, Ni.

The relative energies for each spin state of SnPor-M (M = Fe, Co, Ni, Pt) are reported in table 7.6. For cobalt, spin contamination was significantly observed in the doublet state using unrestricted density functional theory. This leads us to believe that the energy of the doublet state is artificially stable. Attempts to calculate the doublet SnPor-Co with restricted open-shell algorithms, on the other hand, failed to converge. Regardless of its true ground state, binding energies of SnPor-Co for all cases of spin multiplicities were negative (unstable)—even for the artificially stable doublet. Consequently, we can conclude at this point that Co will not deposit stably SnPor and, consequently, SnPor-Co on is not a suitable catalyst material.

Table 7.6. Relative energies versus spin multiplicities of SnPor-M (where M=Pt, Fe, Co and Ni).

Spin multiplicity	Energy (eV)			
	SnPor-Pt	SnPorFe	SnPorCo	SnPorNi
1	0	2.17		0
2			0*	
3	2.53	0		1.29
4			0.45	
5	2.87	1.96		0.83
6			0.33	
7	5.02	1.40		2.66
8			1.61	

*Significant spin contamination.

The relaxed geometries for SnPor-M (M = Pt , Fe, Co, Ni) are summarized in Table 7.7. N plane refers to the average of all possible planes defined three-atom combinations of the four nitrogen atoms. α C refers to the carbons directly bonded to nitrogen. The bond distances between Sn and Fe, Co and Ni are accounted for by the differences in atomic radius between the metals. The relatively small bond distance between Sn and Pt can be attributed to the strong interaction between Pt and SnPor. Our calculations gave energies of 3.13, 1.29, -0.48 and 0.38 eV respectively for the binding of Pt, Fe, Co, Ni on SnPor. For the partial charges of Fe, Ni and Pt in SnPor-M as shown in Table 7.8, electronegativity accounts for the observed trend—i.e., the most electronegative metal, Pt, has the highest partial negative charge.

Table 7.7. Calculated Geometric Parameters of SnPor-M.

Bondlength (Å)	SnPor-Pt	SnPor-Fe	SnPor-Co	SnPor-Ni
M-Sn	2.42	2.63	2.56	2.34
Sn-N Plane	0.82	0.63	0.63	0.86
N1- α C	1.40	1.41	1.41	1.40

Table 7.8. Mulliken charge distribution of neutral SnPor-Pt, SnPor-Fe, and SnPor-Ni and electronegativities of the central metals.

	SnPor-Pt	SnPor-Fe	SnPor-Ni
Por	-1.41	-1.41	-0.99
Sn	0.78	1.41	1.29
M	-0.63	0.0	-0.30

To account for the binding energy of M on SnPor, we calculated the binding energy of Sn atom with metal atoms, M. We found a direct relationship between the binding energy of M on Sn atom and M on SnPor. We performed calculations additional metals as shown in Table 7.9 to confirm our findings. We can conclude that the binding energy of M on SnPor is primarily dependent on its binding energy with atomic Sn.

Table 7.9. Binding Energy (eV) of Sn-M versus SnPor-M, where M=Pt, Ni, Fe, Co

and other metals.

	Sn-M	SnP-M
Pt	-4.4428	-3.1343
Cu	-1.83464	-1.35094
Fe	-2.1065	-1.29675
Ag	-1.57368	-0.42231
Ni	-1.49946	-0.383
Pd	-2.26022	-1.67032
Ir	-5.05056	-3.40367
Au	-2.42482	-1.08041

The frontier molecular orbitals of SnPor-Pt and SnPor-Ni are compared in Figure 7.9. As can be seen from the figure, the frontier molecular orbital wave functions of SnPor-Pt and SnPor-Ni are quite similar except the valence d-electron of Ni is from 3d shells and those of Pt is from 5d shells. This explains the differences in energy gaps between the frontier molecular orbitals of SnPor-Pt and SnPor-Ni. The d-orbitals of the central Ni and Pt atoms are shown to predominate near HOMO and LUMO levels. The frontier molecular orbitals of SnPor-Fe (Figure 7.10), on the other hand, are very different from SnPor-Ni and SnPor-Pt because of the singly-filled d-orbitals of Fe.

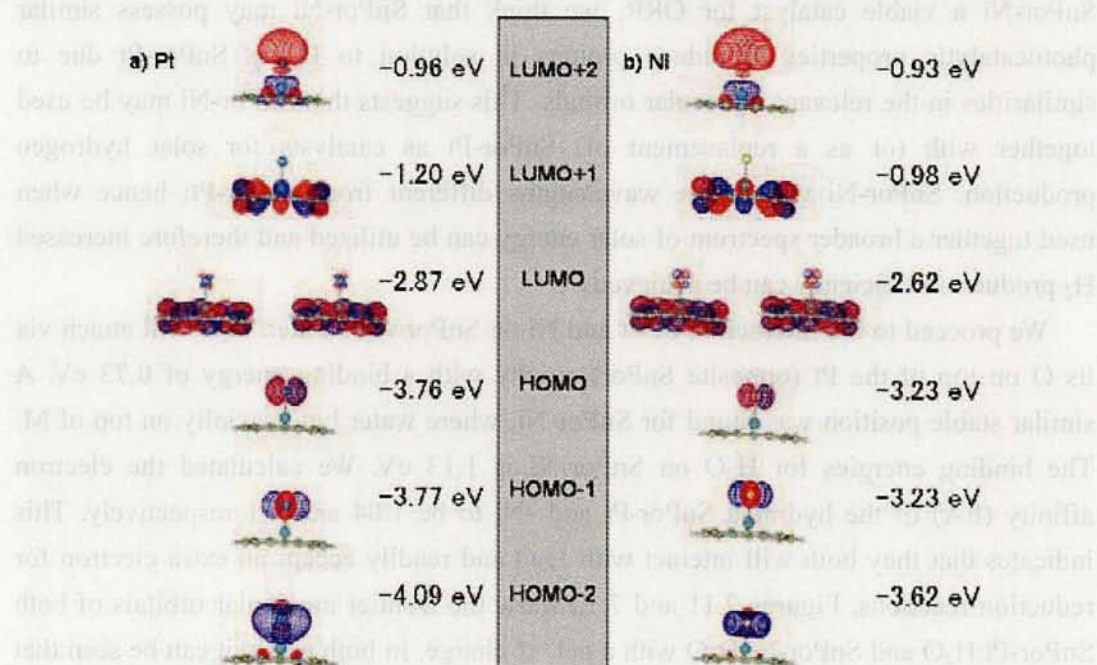


Figure 7.9. Side-by-side comparison of frontier molecular orbitals of SnPor-Pt (a) and SnPor-Ni (b).



Figure 7.10. The frontier molecular orbital of SnPor-Fe.

While the binding the binding energy of Ni on SnPor is not high enough to make SnPor-Ni a viable catalyst for ORR, we think that SnPor-Ni may possess similar photocatalytic properties to reduce protons in solution to H_2 as SnPor-Pt due to similarities in the relevant molecular orbitals. This suggests that SnPor-Ni may be used together with (or as a replacement of) SnPor-Pt as catalysts for solar hydrogen production. SnPor-Ni will utilize wavelengths different from SnPor-Pt; hence when used together a broader spectrum of solar energy can be utilized and therefore increased H_2 production efficiency can be achieved.

We proceed to the interaction of Pt and Ni on SnPor with water. H_2O will attach via its O on top of the Pt (opposite SnPor) axially with a binding energy of 0.73 eV. A similar stable position was found for SnPor-Ni, where water binds axially on top of M. The binding energies for H_2O on SnPor-Ni is 1.13 eV. We calculated the electron affinity (EA) of the hydrated SnPor-Pt and -Ni to be 1.04 and 2.1 respectively. This indicates that they both will interact with H_2O and readily accept an extra electron for reduction reactions. Figures 7.11 and 7.12 show the frontier molecular orbitals of both SnPor-Pt- H_2O and SnPor-Ni- H_2O with a net -1 charge. In both cases, it can be seen that the extra electron (in the HOMO) can transfer from the porphyrin to the hydrogen atoms of H_2O by excitation from the HOMO to the LUMO+1. For SnPor-Pt- H_2O , the

excitation energy is of 2.19 corresponding to an excitation at 565 nm. The similarities between the frontier molecular orbitals of $\text{SnPor-Pt}\cdot\text{H}_2\text{O}^{-1}$ and $\text{SnPor-Ni}\cdot\text{H}_2\text{O}^{-1}$ again supports our idea that SnPor-Ni may have similar photocatalytic properties as SnPor-Pt for H_2 production from H_2O . The main difference is that the excitation energy needed to transfer the HOMO electron from the porphyrin ring to the hydrogen atoms of water in (LUMO+1) is lower (1.47 eV). It corresponds to longer wavelengths of the electromagnetic spectrum (843 nm), but this is not a problem as sunlight, our preferred excitation source for H_2 gas generation, emits radiation significantly in this region.

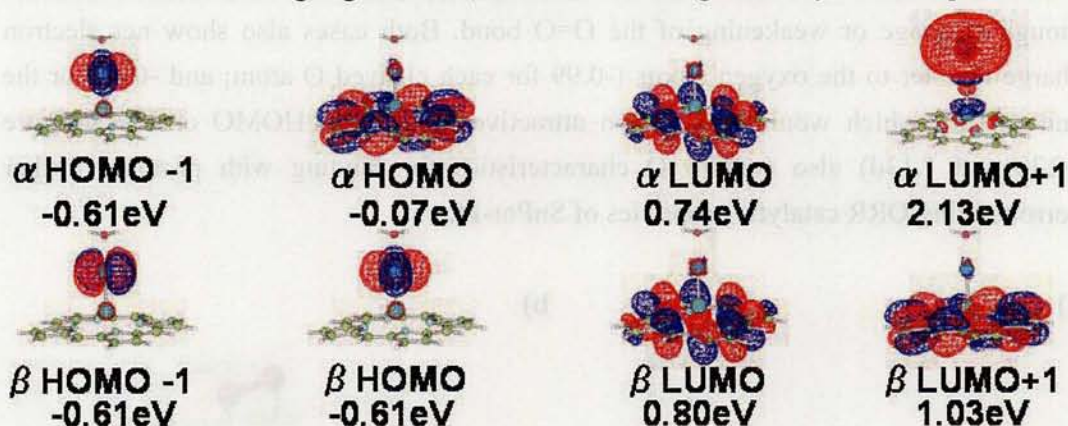


Figure 7.11. Frontier molecular orbitals of $\text{SnPor-Pt}^{-1} \cdot \text{H}_2\text{O}$.



Figure 7.12. Frontier molecular orbitals of $\text{SnPor-Ni}^{-1} \cdot \text{H}_2\text{O}$.

7.4 Interaction of SnPor-Pt with O_2

We consider the interaction of SnPor-Pt with O_2 as a first step to evaluate the feasibility of using SnPor-Pt as an ORR catalyst. We considered both side-on and

end-on interaction. The side-on interaction shows cleavage of the O₂ bond as shown in Figure 7.13a with a binding energy of 1.81 eV (i.e., 0.9 eV per O atom); the heat of adsorption of O on platinum surface is about 250kJ/mol (2.59 eV) [13]. The vibrational frequency for Pt-O (793.4986 cm⁻¹) is much weaker than that of gaseous O₂ (1633.9269 cm⁻¹). On the other hand, the end-on interaction of O₂ with SnPor-Pt (Figure 7.13.b) shows O-O bond elongation (1.27 Å) with a vibrational frequency of 1266.49 cm⁻¹ and binding energy of 0.77eV. The bond length of gaseous O₂ using the same calculation parameters is 1.21 Å. In both cases, ORR catalytic properties of SnPor-Pt are exhibited though cleavage or weakening of the O=O bond. Both cases also show net electron charge transfer to the oxygen atoms (-0.99 for each cleaved O atom; and -0.45 for the end-on O₂), which would make them attractive to protons. HOMO orbitals (Figure 7.13c and 7.13d) also contain O characteristics for binding with protons, further corroborating ORR catalytic properties of SnPor-Pt.

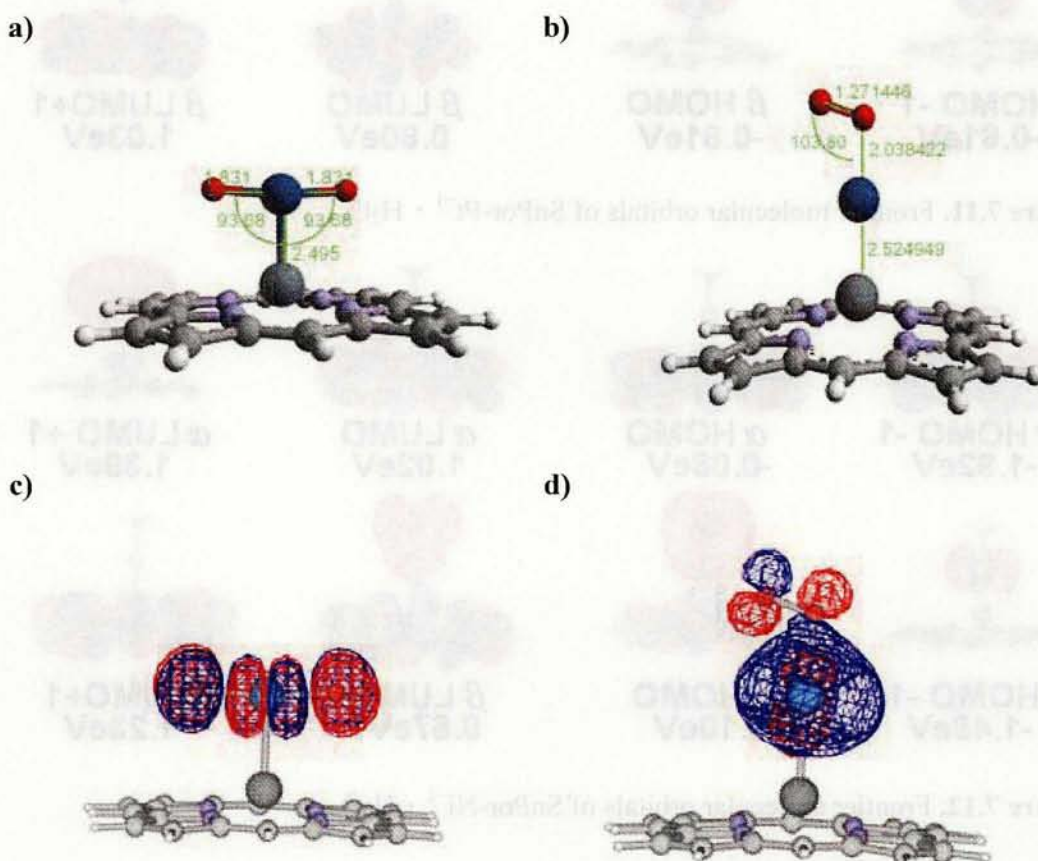


Figure 7.13. Side-on and end-on interaction of O₂ with SnPor-Pt. (a) and (b) show their respective geometry, while (c) and (d) show their respective HOMOs.

Chapter 8

Conclusion

The biggest obstacle to the wide spread use of hydrogen fuel cells is cost—primarily due to the cost of the precious metal Pt, which has been the preferred material for anodes and cathodes across most types of fuel cells. Many studies have been made on how to reduce the amount of platinum in catalysts. But no efficient and stable alternative has been found.

Yet contrary to our present platinum-based technology, nature has its own way of oxidizing hydrogen and reducing oxygen without the need for expensive rare metals. With this in mind, we surveyed literature regarding the ORR and HOR on platinum as well as on heme and hydrogenase. As it turned out, density functional theory (DFT) played an important part in our current understanding of the ORR and HOR processes, whether as applied in industrially-used platinum-based systems or to biologically-present enzyme systems. From there, we took DFT a step further—from its proven applicability in helping us understand HOR/ORR reaction mechanisms to using it as a tool to help us design catalysts inspired by natural enzymes that perform parallel reactions.

The objective of our design efforts for both the anode and cathode is the same: to develop effective and stable alternative electrodes that will eliminate or minimize the use of platinum, but surrounding issues are quite different. For the anode, artificial hydrogenase mimics that are catalytically active are already available, but not as electrodes due to the unavailability of a stable solid state support. For the cathode, synthetic heme based electrodes are available but not efficient enough and/or stable enough for repeated ORR cycles.

Our design efforts led us to propose SnPor-Pt as ORR catalysts. We showed how this material possesses the necessary electronic properties that make it a possible alternative to the platinum surfaces as fuel cell electrode catalyst. The calculated binding energy of Pt on SnPor is 3.13 eV—very stable. We showed how this material possesses the necessary electronic properties that make it a possible alternative to platinum surfaces as fuel cell electrode catalysts; notably: low electron density near Pt, partial negative charge at Pt, and the high Pt-character near and at HOMO levels. The LUMO also possess significant Pt d-orbital characteristics comparable to the α - and β -LUMO of iron porphyrin, further suggesting ability to interact with oxygen for catalytic reduction.

We also considered replacing tin with germanium (Ge) and lead (Pb). Pt deposited on GePor shows primarily the same results as SnPor-Pt, but Pt deposited PbPor shows a

much weaker binding energy (1.99 eV). Variants of SnPor-Pt by replacing Pt with nickel (Ni), cobalt (Co), and iron (Fe) were also studied. Our calculations gave energies of 1.29, -0.48 and 0.38 eV respectively for the binding of Fe, Co and Ni on SnPor. We compared their electronic properties with SnPor-Pt, hoping that these non-precious metals on SnPor will also possess the needed electronic properties for PEFC HOR or ORR catalysis. While the binding energy of Ni on SnPor is not high enough to make SnPor-Ni a viable catalyst for ORR, the similarities between their frontier molecular orbitals suggest that SnPor-Ni may have similar photocatalytic properties as SnPor-Pt for H₂ production in aqueous solution.

For the anode, we showed how changing ligands affects the electronic structure of hydrogenase active site analogues. From the standpoint of computational materials design, it can be seen that changing ligands will primarily affect the charge distribution and HOMO/LUMO wave function/energy levels of 2Fe₂S clusters. We therefore think that similarities in 2Fe charge density and HOMO/LUMO characteristics to the biologically present active site should be bases for predicting catalytic activity of Fe-only hydrogenase analogues.

As a first attempt to hold the [2Fe]_H active site in solid state, we consider thiol derivatives of calixarenes as possible scaffolds. Among the calixarenes so far considered, our calculations has shown that calix[5]arene is the most viable macrocycle to hold the di-iron site. Our calculations also show that the crucial hydrogenase active site is maintained in this material: having an Fe-Fe bond and anti-bond at the HOMO and LUMO respectively (Figure 6.8); and the bonding orbitals on the Fe centers connected to the sulfur of the electron chain at the HOMO.

Ultimately, the materials we design need to be synthesized in the laboratory and tested for efficiency to perform HOR/ORR and for long-term stability. We are, at present, doing so in collaboration with synthetic chemists. Our tasks of computational material design bore fruits. The question that critics will always ask is: “what if these synthetic efforts fail to realize the new material and properties we predicted?” Our answer to that is: First, the fact we have communicated to experimentalists which materials are energetically possible to synthesize and which are not even worth trying is in itself already significant output—just consider the additional amount of chemicals, electricity, equipment, effort, time and waste disposal expenses that otherwise would have been spent. With the guidance of density functional calculations, we have significantly narrowed down our choices and need not work by trial and error to arrive at something useful. Second, in our quest for knowledge, whatever result that comes out of our synthetic and testing efforts will never be a “failure”—it is only either the

“expected” or “unexpected”. Provided that we analyze the synthesis results properly and continue our design-analyze-synthesize-analyze cycle of research, the very least we can gain is improving our materials design techniques—both experimentally and computationally.

References:

- 1) Graham A P, Menzel A and Toennies J P 1999 *J. Chem Phys.* **111** 1676-85.
- 2) Roman T, Nakanishi H, Diño W A and Kasai H 2006 *e-J. Surf. Sci. and Nanotech.* **4** 619-23.
- 3) Chen J and Chan K-Y 2005 *Molecular Simulation* **31** 527-533.
- 4) Chan K-Y, Ding J, Ren J, Cheng S and Tsang K Y 2004 *J. Mater. Chem.* **14** 505-516.
- 5) Tsuda M, Diño W A and Kasai H, 2005 *Solid State Comm.* **133** 589-591.
- 6) Tsuda M, Diño W A, Nakanishi H and Kasai H 2004 *e-Journal of Surface Science and Nanotechnology* **2** 226-229; Dy E S, Diño W A, Tsuda M and Kasai H 2005 *e-Journal of Surface Science and Nanotechnology* **3** 233-236.
- 7) Thauer R K 1998 *Microbiology* **144** 2377-2406.
- 8) Vignais P M, Billoud B and Meyer J 2001 *FEMS Microbiol. Rev.* **25** 455-501.
- 9) Adams M W W and Stiefel E I 1998 *Science* **282** 1842-1843.
- 10) Frey M 2002 *ChemBioChem* **3** 153-160.
- 11) Markovic N M, Grgur B N, and Ross P N 1997 *J. Phys. Chem. B*, **101**, 1997, 5405 – 5413.
- 12) Markovic N M and Ross P N 1999 *Interfacial Electrochemistry: Theory, Experiment and Applications*, ed Wieckowski A (Marcel Dekker, New York) 821-841.
- 13) Markovic N M and Ross P N 2002 *Surf. Sci. Rep.* **45** 117-229.
- 14) Christmann K 1998 *Electrocatalysis*, ed. Lipkowski J and Ross P N (Wiley-VCH, New York) 1-42. (Book)
- 15) Olsen RA, Kroes GJ, Baerends EJ 1999 *J. Chem. Phys.* **111** 11155.
- 16) Norton P R, Da Vies J A, Creber D K, Sitter C W and Jackman T E 1981 *Surface Science* **108** 205-224.
- 17) B. Pennemann, K. Oster and K. Wandelt, 1991 *Surface Science* **249** 35-43.
- 18) Hu X and Lin Z 1995 *Phys. Rev. B* **52** 11467-11471.
- 19) Lee W T, Ford L, Blowers P, Nigg H L and Masel R I 1998 *Surface Science* **416** 141-151.
- 20) Krishtalik L I 1970 *Advances in Electrochemistry and Electrochemical Engineering Vol. 7*, ed P. Delahay, (Interscience, New York) 1970.
- 21) Parson R 1958 *Trans. Faraday Soc.* **54** 1053-1063
- 22) Trasatti S 1972 *J. Electroanal. Chem.* **39** 163-184.
- 23) Trasatti S 1997 *Surface Science* **335** 1-9.
- 24) Nørskov J K, Bligaard T, Logadottir A, Kitchin J R, Chen J G, Pandelov S and Stimming U, 2005 *J Electrochem. Soc.* **152** J23-J26.
- 25) Wroblowa H, Pan Y C, Razumney G 1976 *J. Electroanal. Chem.* **69** 195-201.

- 26) Gland J L, Sexton B A, Fisher GB 1980 *Surf. Sci.* **95** 587-602.
- 27) Dicke J, Rotermund H H, Lauterbach J 2000 *Surf. Sci.*, **454** 352-357 and references quoted therein.
- 28) Eichler A and Hafner J 1997 *Phys. Rev. Lett.* **79** 4481-4484.
- 29) Yotsuhashi S, Yamada Y, Diño WA, Nakanishi H and Kasai H 2005 *Physical Review B* **72** 033415.
- 30) Eiswirth M, Möller P, Wetzl K, Imbihl R and Ertl G 1989 *J. Chem. Phys.* **90** 510-521.
- 31) Cox M P, Ertl G, and Imbihl R 1985 *Phys. Rev. Lett.* **54** 1725-1728.
- 32) Rotermund H H, Engel W, Kordesch M and Ertl G 1990 *Nature (London)* **343** 355.
- 33) Markovic N, Gasteiger H, Ross P 1997 *J. Electrochem. Soc.* **144** 1591-1597.
- 34) Gojkovic S L, Savinell R F, 1997, *J. Electrochem. Soc.* **144** 2973-2979.
- 35) Chen S, Kucernak A, 2004, *J. Phys. Chem. B*, **108**, 3262-3276
- 36) Paulus UA, Schmidt TJ, Gasteiger HA, Behm RJ 2001 *Journal of Electroanalytical Chemistry* **495** 134–145.
- 37) Dhanda A, O’Hayre R, Pitsch H, 2006 *210th ECS Meeting, Abstract* #1958.
- 38) Ekström H, Hanarp P, Gustavsson M, Fridell E, Lundblad A, Lindbergh G, 2006 *J. Electrochem. Soc.*, 2006, **153**(4), A724-A730).
- 39) Anderson A B and Albu TV 2000 *J. Electrochem. Soc.* **147** (11) 4229-38.
- 40) Sidik R A and Anderson A B 2002 *J. Electroanal. Chem.* **528** 69-76.
- 41) Nørskov J K, Rossmeisl J, Logadottir A, Lindqvist L, Kitchin J R, Bligaard T and Jonsson H 2004 *J. Phys. Chem. B* **108** 17886-92.
- 42) Shi Z, Zhang J, Liu Z-S, Wang H and Wilkinson D P 2006 *Electrochimica Acta* **51** 1905–1916.
- 43) Armstrong F 2004 *Current Opinion in Chemical Biology* **8** 133-140.
- 44) Cammack R 1999 *Nature* **397** 214-215.
- 45) Nicolet Y, Piras C, Legrand P, Hatchikian C E, Fontecilla-Camps J E C 1999 *Structure* **7** 13-23.
- 46) Peters J W, Lanzilotta W N, Lemon B J, Seefeldt L C 1998 *Science* **282** 1853-1858.
- 47) Pierik A J, Hulstein M, Hagen W R, Albracht S P J 1998 *Eur. J. Biochem.* **258** 572-578.
- 48) Chen Z, Lemon B J, Huang S, Swartz D J, Peters J W, and Bagley K A, 2002 *Biochemistry* **41** 2036-2043.
- 49) Rusnak F M, Adams M W E, Mortenson L E, and Münck E, 1987 *J. Biol. Chem.* **262** 38-41.
- 50) Zambrano I C, Kowal A T, Mortenson L E, Adams M W W, and Johnson M K 1989

J. Biol. Chem. **264** 20974-20983.

51) Pierik A J, Hagen W R, Redeker J S, Wolbert R B G, Boersma M, Verhagen M F J M, Grande H J, Vebger C, Mutsaers P H A, Sands R H and Dunham W R 1992 *Eur. J. Biochem.* **209** 63 – 72.

52) Adams M W W 1987 *J. Biol. Chem.* **262** 15054-15061.

53) Adams M W W and Mortenson L E 1984 *J. Biol. Chem.* **259** 7045-7055.

54) Popescu C V and Münck E 1999 *J. Am. Chem. Soc.* **121** 7877-7884.

55) Schmidt M, Contakes S M and Rauchfuss T B 1999 *J. Am. Chem. Soc.* **121** 9736-9737.

56) Le Cloirec A, Best S P, Borg S, Davies SC, Evans D J, Hughes D L and Pickett C J 1999 *Chem. Commun.* 2285–2286.

57) Cao Z and Hall M 2001 *J. Am. Chem. Soc.* **123** 3734-3742.

58) Evans D J and Pickett CJ 2003 *Chem. Soc. Rev.* **32** 268-275.

59) Darensbourg M Y, Lyon E J, Zhao X and Georgakaki IP 2003 *Proc. Nat. Acad. Sci.* **100** 3683-3688.

60) Fan H J and Hall M B 2001 *J. Biol Inorg Chem.* **6** 467-473.

61) Liu ZP and Hu P 2002 *J. Am. Chem Soc* **124** 5175-5182.

62) Zhou T, Mo Y, Liu A, Zhou Z and Tsai K R 2004 *Inorganic Chemistry* **43** 923-930.

63) Georgakaki I P, Thomson L M, Lyon E J, Hall M B and Darensbourg M Y 2003 *Coord. Chem. Rev.* **238-239** 255-266.

64) Greco C, Bruschi M, De Gioia L and Ryde U 2007 *Inorganic Chemistry*, published in the web 6/29/2007, 10.1021/ic06232a

65) Ezzaher S, Capon J-F, Gloaguen F, Pétillon F Y, Schollhammer P and Talarmin J, 2007 *Inorganic Chemistry* **46** 3426-3428.

66) Rauchfuss T B 2004 *Inorg. Chem.* **43** 14-26.

67) Capon, J-F, Gloaguen F, Schollhammer P, Talarmin J 2005 *Coord. Chem. Rev.* **249** 1664-1676.

68) Schwartz L, Eilers G, Eriksson L, Gogoll A, Lomoth R and Ott S 2006 *Chem. Commun.* 520–522.

69) Schmidt M, Contakes S M and Rauchfuss T B 1999 *J. Am. Chem. Soc.* **121** 9736-9737; Lawrence JD, Li H and Rauchfuss T B, 2001 *Chem. Comm.* 1482-1483.

70) Gloaguen F, Lawrence J D, Rauchfuss T B 2001 *J. Am. Chem. Soc.* **123**, 9476-9477.

71) Tard C, Liu X, Ibrahim S K, Bruschi M, De Gioia L, Davies SC, Yang X, Wang L-S, Sawers G and Pickett C J 2005 *Nature* **433** 610-612.

72) Nakanishi H, Miyamoto K, David M, Dy E, Tanaka R and Kasai H 2007 *J. Phys: Condens.* **19** 365234-5.

- 73) Proniewicz L M, Paeng I R and Nakamoto K 1991 *J. Am. Chem. Soc.* **113** 3294-303.
- 74) Woolery G L, Walters M A, Suslick K S, Powers L S and Spiro T G 1985 *J. Am. Chem. Soc.* **107** 2370-3.
- 75) Bajdor K, Oshio H and Nakamoto K 1984 *J. Am. Chem. Soc.* **106** 7273-4.
- 76) Rovira C, Kunc K, Hutter J, Ballone P and Parrinello M 1997 *J. Phys. Chem. A* **101** 8914-25.
- 77) Dawson J H, Holm R H, Trudell J R, Barth G, Linder R E, Bunnenberg E, Djerassi C and Tang S C 1976 *J. Am. Chem. Soc.* **98** 3707-9.
- 78) Tsuda M, Dy E S and Kasai H 2005 *J. Chem. Phys.* **122** 244719.
- 79) Collman J P, et al, 1974 *Proc. Nat. Acad. Sci. USA* **71** 1326-1329.
- 80) Vogel K M, Kozlowski P M, Zgierski M Z, Spiro T G 1999 *J. Am. Chem. Soc.* **121** 9915-9921; Blomberg L M, Blomberg M R A, and Siegbahn P E M 2005 *J. Inorg. Biochem.* **99** 949–958; and references therein.
- 81) Rovira C, Parinello M, 2000 *Int. J. of Quantum Chem.* **80** 1172-1180; Rovira C 2003 *J. Phys.: Condens. Matter* **15** S1809–S1822.
- 82) Momenteau M, Reed C A 1994 *Chem. Rev.* **94** 659-698.
- 83) Silaghi-Dumitrescu R 2004 *J. Biol. Inorg. Chem.* **9** 471-476 and references cited therein.
- 84) Han S, Ching Y-C, Rousseau D L 1990 *Nature* **348** 89–90. (library)
- 85) Springer B A, Sligar S G, Olson J S, Phillips G N Jr. 1994 *Chem. Rev.* **94** 699-714.
- 86) Spiro T G, Kozlowski P M 2001 *Acc. Chem. Res.* **34** 137; Spiro TG, Zgierski M Z, Kozlowski P M 2001 *Coordination Chemistry Reviews* **219–221** 923–936.
- 87) Collman J P, Boulatov R, Sunderland C J, Fu Lei, 2004, *Chem. Rev.* **104** 561-588.
- 88) Tarasevich M R, Sadkowsky A and Yeager E. 1983 *Comprehensive Treatise of Electrochemistry, Vol. 7.* ed Bockris J O'M, Conway B E, Yeager E., Khan S U M, White R E (Plenum, New York), 301-398.
- 89) Tanaka A A, Fierro C, Scherson D and Yeager E B 1987 *J. Phys. Chem.* **91** 3799-807.
- 90) Lai M E and Bergel A 2000 *J. Electroanal. Chem.* **494** 30-40; Maruyama J and Abe I 2005 *Chem. Mater.* **17** 4660-7.
- 91) Zhang L, Song C, Zhang J, Wang H and Wilkinson D P 2005 *J. Electrochem. Soc.* **152** A2421-A2426; erratum, 2006, **153** L7-L7.
- 92) Tsuda M, Dy E S and Kasai H 2006 *Eur. Phys. J. D* **38** 139-141.
- 93) Aquilanti V, Ascenzi D, Cappelletti D, Pirani F, 1994 *Nature* **371** 399-402.
- 94) Aquilanti V, Ascenzi D, Cappelletti D, Pirani F, 1995 *J. Phys. Chem.* **99**

13620-13626

- 95) Aquilanti V, Bartolomei M, Pirani F, Cappelletti D, Vecchiocattivi F, Simizu Y, Kasai T, 2005 *Phys. Chem. Chem. Phys.* **7** 291-300.
- 96) Tsuda M, Diño W A and Kasai H 2005 *Jpn. J. Appl. Phys.* **44** L57-9.
- 97) Yoshikawa S, Shinzawa-Itoh K, Nakashima R, Yaono R, Yamashita E, Inoue N, Yao M, Fei M J, Libeu C P, Mizushima T, Yamaguchi H, Tomizaki T, Tsukihara T 1998 *Science* **280** 1723-1729.
- 98) Tsuda M, David M, Kasai H 2006 *Surf. Sci.* **600** 3992-3994.
- 99) Collman JP, Devaraj NK, Decréau R A, Yang Y, Yan Y L, Ebina W, Eberspacher T A, Chidsey C E D, 2007, *Science*, **315**, 1565-1568 and references quoted therein.
- 100) Kubota Y, Dy E S, Nakanishi H, Kasai H and Diño W A 2006 *e-J. Surf. Sci. Nanotech.* **4** 630-5.
- 101) Tachibana J, Imamura T and Sasaki Y, 1998 *Bull. Chem. Soc. Jpn.* **71** 363-9.
- 102) Fujihara T, Sasaki Y, Imamura T 1999 *Chem. Lett.* **28** 403-404.
- 103) Fujihara T, Rees N H, Umakoshi K, Tachibana J, Sasaki Y, McFarlane W and Imamura T 2000 *Chem. Lett.* **29** 102-103.
- 104) Gaussian 03, Revision D.02, M. J. Frisch, G. W. Trucks, H. B. Schlegel, G. E. Scuseria, M. A. Robb, J. R. Cheeseman, J. A. Montgomery, Jr., T. Vreven, K. N. Kudin, J. C. Burant, J. M. Millam, S. S. Iyengar, J. Tomasi, V. Barone, B. Mennucci, M. Cossi, G. Scalmani, N. Rega, G. A. Petersson, H. Nakatsuji, M. Hada, M. Ehara, K. Toyota, R. Fukuda, J. Hasegawa, M. Ishida, T. Nakajima, Y. Honda, O. Kitao, H. Nakai, M. Klene, X. Li, J. E. Knox, H. P. Hratchian, J. B. Cross, V. Bakken, C. Adamo, J. Jaramillo, R. Gomperts, R. E. Stratmann, O. Yazyev, A. J. Austin, R. Cammi, C. Pomelli, J. W. Ochterski, P. Y. Ayala, K. Morokuma, G. A. Voth, P. Salvador, J. J. Dannenberg, V. G. Zakrzewski, S. Dapprich, A. D. Daniels, M. C. Strain, O. Farkas, D. K. Malick, A. D. Rabuck, K. Raghavachari, J. B. Foresman, J. V. Ortiz, Q. Cui, A. G. Baboul, S. Clifford, J. Cioslowski, B. B. Stefanov, G. Liu, A. Liashenko, P. Piskorz, I. Komaromi, R. L. Martin, D. J. Fox, T. Keith, M. A. Al-Laham, C. Y. Peng, A. Nanayakkara, M. Challacombe, P. M. W. Gill, B. Johnson, W. Chen, M. W. Wong, C. Gonzalez, and J. A. Pople, Gaussian, Inc., Wallingford CT, 2004.
- 105) McQuarrie D A and Simon JD, 1997 *Physical Chemistry A molecular Approach* (University Science Books, CA) pp 275-307; Cook D B 2005 *Handbook of Computational Quantum Chemistry* (Dover, New York).
- 106) Kock W and Holthausen 2001 *A Chemist's Guide to Density Functional Theory, 2nd Edition* (Wiley-VCH).
- 107) Hohenberg P and Kohn W 1964 *Phys Rev* **136** B864-B871.

- 108) Kohn W and Sham L J 1965 *Physical Review* **140** A1133-A1138.
- 109) Kohn W, *Nobel Price Lecture*, June 28, 1999.
- 110) Kohn W, Becke A D, and Parr R G 1996 *J. Phys. Chem.* **100** 12974-12980.
- 111) Vosko S H, Wilk L and Nusair M 1980 *Can. J. Phys.* **58** 1200 (1980)
- 112) Ceperly D M and Alder B J 1980 *Phys. Rev. Lett.* **45** 566-569.
- 113) Becke A D 1988 *Phys. Rev. A* **38** 3098(1988).
- 114) Perdew J P 1985 *Phys. Rev. Lett* **55** 1665; Perdew J P and Wang Y 1986 *Phys. Rev. B* **33** 8800.
- 115) Lee C, Yang W and Parr R G 1988 *Phys. Rev. B* **37** 785-789.
- 116) Perdew J P 1986 *Phys. Rev. B* **33** 8822; erratum 34,7406.
- 117) J. P. Perdew, K. Burke, and Y. Wang 1996 *Phys. Rev. B* **54** 16533.
- 118) Stephens P J, Devlin FJ, Chabalowski C F and Frisch M J 1994 *J. Phys. Chem.* **98** 11623-11627.
- 119) Becke A D 1993 *J. Chem. Phys.* **98** 5648-5652.
- 120) EMSL Gaussian Basis Set Order Form
(<http://www.emsl.pnl.gov/forms/basisform.html>) based on the works of: Hariharan P C and Pople J A 1973 *Theoret. Chimica Acta* **28** 213; Franci M M, Pietro W J, Hehre W J, Binkley J S, Gordon M S, DeFrees D J and Pople J A, 1982 *J. Chem. Phys.* **77**, 3654; Clark T, Chandrasekhar J, Schleyer PVR 1983 *J. Comp. Chem.* **4**, 294. Krishnam R, Binkley J S, Seeger R, Pople J A 1980 *J. Chem. Phys.* **72** 650; Gill P M W, Johnson B G, Pople J A and Frisch J 1992 *Chem. Phys. Lett.* **197** 499. Frisch M J, Pople J A, and Binkley J S, *J. Chem. Phys.* **80**, 3265 (1984); Unpublished data from Gaussian 94 [Ref. 104].
- 121) EMSL Gaussian Basis Set Order Form
(<http://www.emsl.pnl.gov/forms/basisform.html>) based on the works of: Dunning T H Jr. and Hay P J 1977, *Methods of Electronic Structure, Theory, Vol. 2*, H. F. Schaefer III, ed., (Plenum Press) ; Hay P J and Wadt W R 1985 *J. Chem. Phys.* **82**, 270 (1985). Hay P J and Wadt W R 1985 *J. Chem. Phys.* **82**, 284. Hay P J and Wadt W R 1985 *J. Chem. Phys.* **82** 299. Ortiz J V, Hay P J and Martin R L 1992 *J. Am. Chem. Soc.* **114** 2736 and **114** 2736; Dunning T H Jr. and Hay P J 1976 *Modern Theoretical Chemistry, Vol. 3* (Plenum, New York) Ed. H. F. Schaefer III, 1-28.
- 122) Dy E S, Kasai H, Redshaw C and Pickett C, *E-J. Surf. Sci. and Nanotech.*, **5**, 148-151.
- 123) Yang X, Razavet M, Wang X B, Pickett C J and Wang L S 2003, *J. Phys. Chem. A* **107**, 4612-4618.
- 124) Rienstra-Kiracofe J C, Tschumper G S, Schaefer III H F, Nandi S and Ellison G B,

2002 *Chem. Rev.* **102**, 231-282.

125) Anderson E L, Fehlner T P, Foti A E and Salahub D R 1980, *J. Am. Chem. Soc.* **102**, 7429-7433; Teo B K, Hall M B, Fenske R F and L. F. Dahl 1975, *Inorg. Chem.* **14**, 3103-3117.

126) Dy E S, Kasai H and Redshaw C “Designing A Calixarene Solid State Support For The Hydrogenase Active Site”, *Surface and Interface Analysis*, submitted.

127) Karakhanov E A, Buchneva T S, Maksimov A L, Runova E A, 2003 *Petroleum Chemistry* **43** 38–45.

128) Gutsche C D, Calixarenes, *Monographs in Supramolecular Chemistry*, ed. J. Frasier Stoddart, Royal Society of Chemistry; New Ed edition (June 1993) 978-0851863856.

129) Andreetti G D, Ungaro R and Pochini A 1979 *Chem. Commun.* 1005 – 1007.

130) Coruzzi M, Andreetti G D, Bocchi V, Pochini A and Ungaro R 1982 *J. Chem. Soc., Perkin Trans. 2* 1133 – 1138.

131) Olmstead M M, Sigel G, Hope H, Xu X and Power P P 1985 *J. Am. Chem. Soc.* **107** 8087-8091.

132) R. M. Izatt, J. J. Christensen, R. T. Hawkins, U.S. Patent 4,477,377, 16 Oct 1984 (Chem. Abstr., 101:21833m)

133) Hitachi Chemical Co., Lt., Jpn. Kokai Tokkyo Koho, JP 59,104,331, 1984 (Chem. Abstr. 101: 191410); *ibid.*, JP 59,12,913, 1984 (Chem. Abstr. 101:24477); *ibid.*, JP 59,12915, 1984 (Chem. Abstr., 101:8163); *ibid.*, 60,202,113, 1984 (Chem. Abstr. 104: 207904); *ibid.*, JP 61,106,775, 1986 (Chem. Abstr., 105:231158k) ; Y. Nakamoto, S. Ishida, Y. Yoshimura (Hitachi Chemical Co., Ltd.), Jpn. Kokai Tokkyo Koho, JP 62,96,505, 1987 (Chem. Abstr., 108: 56797f); *idem.*, *ibid.*, 62, 96,440, 1987, Chem. Abstr., 108:6959q

134) S. Shinkai, O. Manabe, Y. Kondo, T. Yamamoto (Kanebo, Ltd.), Jpn. Kokai Tokkyo Koho, JP 62, 136,242, 1987 (Chem. Abstr. 108: 64410q); Y. Kondo, T. Yamamoto, O. Manabe, S. Shinkai (Kanebo, Ltd.), Jpn. Kokai Tokkyo Koho, JP 62,210,055, 1987 (Chem. Abstr. 108: 116380b)

135) Lyon E J, Georgakaki I P, Reibenspies J H, Darensbourg M Y 1999 *Angew. Chem., Int. Ed.* **38** 3178-3180.

136) Rauchfuss T B, Contakes S M and Schmidt M 1999 *J. Am. Chem. Soc.* **121** 9736-9737.

137) Landrum J T, Amini M, Zuckerman J J 1984 *Inorg. Chim. Acta* **90** L73-L74.

138) Barbe J-M, Ratti C, Richard P, Lecomte C, Gerardin R, Guillard R 1990 *Inorg. Chem.* **29** 4126-4130.

- 139) Onaka S, Kondo Y, Yamashita M, Tatematsu Y, Kato Y, Goto M and Ito T 1985 *Inorg. Chem.* **24** 1070-6.
- 140) Barbe J-M, Guillard R, Lecomte C and Gerardin R 1984 *Polyhedron* **3** 889-94.
- 141) Onaka S, Kondo Y, Toriumi K and Ito T 1980 *Chem. Lett.* 1605-08.
- 142) Kadish K M, Swistak C, Boisselier-Cocolios B, Barbe J-M and Guillard R 1986 *Inorg. Chem.* **25** 4336-43.
- 143) Guillard R, Fahim M, Zaegel F, Barbe J-M, d'Souza F, Atmani A, Adamian V A, Kadish K M 1996 *Inorg. Chim. Acta* **252** 375-82.
- 144) Noda I, Kato S, Mizuta M, Yasuoka N, Kasai N 1979 *Angew. Chem. Int. Ed. Engl.* **18** 83.
- 145) Wang S, Tabata I, Hisada K and Hori T 2002 *Dyes and Pigments* **55** 27-33
- 146) Wang Z, Medforth C J and Shelnutt J A 2004 *J. Am. Chem. Soc.* **126** 16720-1
- 147) Song Y, Steen W A, Peña D, Jiang Y B, Medforth C J, Huo Q, Pincus J L, Qiu Y, Sasaki D Y, Miller J E and Shelnutt J A 2006 *Chem. Mater.* **18** 2335-46.
- 148) Dy E S and H Kasai 2006 *Chem. Phys. Lett.* **422** 539-542.
- 149) Dy E S and H Kasai 2007 *J. Phys. Condens. Matter.* **9** 365240-5.
- 150) Dy E S and H Kasai 2007 *Eur. Phys. J. D* **41** 241-245.

Acknowledgments

I wish to thank my supervisor, Professor Dr. Hideaki Kasai, for his never-tiring instruction and guidance, and for letting me become part of the Kasai Laboratory. For similar reasons, I would also like to thank Professors Dr. Hiroshi Nakanishi and Dr. Wilson Agerico Diño. To the staffs (and former staffs) of Kasai laboratory, namely Ms. Keiko Kobayashi, Ms. Reiko Tanaka, Ms. Akiko Horiguchi, Mr. Shinichi Kunikata, Mr. Hirofumi Kishi, and also Ishioka-San and Matsumoto-San, thank you very much for helping me adjust to a new and very interesting work culture.

To Professors Dr. Gerardo Janairo and Dr. Wyona Patalinghug of De La Salle University, thank you for encouraging and recommending me to pursue this doctorate study; Professors Dr. Emmanuel Rodulfo and Dr. Robert Roleda for helpful lectures; to Professors Dr. Carl Redshaw and Dr. Christopher J Pickett of the University of East Anglia for the first-hand catalyst synthesis experience and for helpful discussions.

I wish to thank The Rotary Yoneyama Memorial Foundation, Inc. for my scholarship and Itsuro Hashimoto Sensei for taking the time and effort to be my adviser.

This work is supported by the Ministry of Education, Culture, Sports, Science and Technology of Japan (MEXT) through their Grant-in-Aid for Scientific Research on Priority Areas (Developing Next Generation Quantum Simulators and Quantum-Based Design Techniques); Special Coordination Funds for the 21st Century Center of Excellence (COE) Program (G18) “Core Research and Advance Education Center for Materials Science and Nano-Engineering” and Grants-in-Aid for Scientific Research programs supported by the Japan Society for the Promotion of Science (JSPS); NEDO Fuel Cell Program; and the Daiwa Anglo-Japanese Foundation. The calculations were done using the computer facilities of the Cybermedia Center (Osaka University) and the Japan Atomic Energy Research Institute (ITBL, JAERI).

List of Publications

1. "Designing A Calixarene Solid State Support For The Hydrogenase Active Site"
Eben Sy Dy, Hideaki Kasai and Carl Redshaw, Surface and Interface Analysis.
2. "A Density Functional Analysis on the Photoelectronic Spectra of Fe-Only Hydrogenase Analogues"
Eben Sy Dy, Hideaki Kasai, Carl Redshaw and Christopher J Pickett, E-Journal of Surface Science and Nanotechnology, 5, 148-151 (2007).
3. "Exploring haem-based alternatives for oxygen reduction catalysis in fuel cells—a status report of our first principles calculations"
Eben Sy Dy, Tanglaw Roman, Yoshiyuki Kubota, Keita Miyamoto and Hideaki Kasai, Journal of Physics: Condensed Matter, 19, 445010 (2007).
4. "A study on the stability of O₂ on oxometalloporphyrins by the first principles calculations"
Yoshiyuki Kubota, Mary Clare Sison Escaño, Eben Sy Dy, Hiroshi Nakanishi and Hideaki Kasai, The Journal of Chemical Physics, 126, 194303 (2007).
5. "A comparative study on the interaction of platinum with group 4A (germanium, tin and lead) porphyrins"
Eben Sy Dy and Hideaki Kasai, Journal of Physics: Condensed Matter, 19, 365240 (2007).
6. "A comparative study on the interaction between tin(II) porphyrin and selected group 8B metals for potential application as reduction catalysts"
Eben Sy Dy and Hideaki Kasai, The European Physical Journal D., 41, 241–245 (2007).
7. "A first principles investigation on the interaction of oxomolybdenum porphyrin with O₂—oxomolybdenum porphyrin as a catalyst for oxygen reduction"
Yoshiyuki Kubota, Eben Sy Dy, Hiroshi Nakanishi, and Hideaki Kasai, e-Journal of Surface Science and Nanotechnology, 4, 630-635 (2006).
8. "First principles study of electric and magnetic properties of benzene-iron multiple-decked sandwich chain"
Md. Mahmudur Rahman, Rifki Muhida, Eben Sy Dy, Romel Mozo and Hideaki Kasai, Journal of the Physical Society of Japan., 75, 114714 (2006).
9. "A theoretical analysis on the interaction between tin(II) porphyrin and platinum and the electronic characteristics of their reaction product"
Eben Sy Dy and Hideaki Kasai, Chemical Physics Letters, 422, 539–542 (2006).
10. "Characterization of platinum porphyrins and its interaction with oxygen by density

functional theory”

Eben Sy Dy and Hideaki Kasai, e-Journal of Surface Science and Nanotechnology, 3, 473-475(2005).

11. “Theoretical investigation of electric and magnetic properties of benzene-vanadium sandwich complex chain”

Md. Mahmudur Rahman, Hideaki Kasai and Eben Sy Dy, Japanese Journal of Applied Physics, 44, 7954–7956(2005).

12. “Characterization of the Im-(Im)PorFe bond by density functional theory”

Eben Sy Dy and Hideaki Kasai, Thin Solid Films, 509, 212-214 (2006).

13. “Bis(histidine)/bis(Imidazole) heme complex—polymer electrolyte fuel cell application as an alternative cathode electrode catalyst”

Eben Sy Dy, Wilson Agerico Dino, Muneyuki Tsuda and Hideaki Kasai, e-Journal of Surface Science and Nanotechnology, 3 233-236 (2005).

14. “Comparative study of O₂ dissociation on various metalloporphyrins”

Muneyuki Tsuda, Eben Sy Dy and Hideaki Kasai, Journal of Chemical Physics, 122, 244719(2005).

15. “Side-on O₂ interaction with heme-based nanomaterials”

Muneyuki Tsuda, Eben Sy Dy and Hideaki Kasai, The European Physical Journal D, 38, 139-141 (2006).

16. “Science and technology III: chemistry. A high school chemistry textbook”, Eben Sy Dy, Magdalena Jauco and Fely Ventura, Rex Bookstore, Copyright 1994.